Pore Scale Methods to Enhance Understanding of Geochemical Reaction Rates in Porous Media

by

Ishan Shrikant Anjikar

A thesis submitted to the Graduate Faculty of
Auburn University
in partial fulfillment of the
requirements for the Degree of
Master of Science

Auburn, Alabama
August 3, 2019

Keywords: 3D Printing, Reactive Transport Modelling, OpenFOAM, X-ray CT

Approved by

Lauren E. Beckingham, Chair, Assistant Professor of Civil Engineering
Jose G. Vasconcelos, Assistant Professor of Civil Engineering
Mark Barnett, Professor of Civil Engineering

Abstract

Geochemical reactions play an important role in subsurface systems such as in contaminant fate and transport, chemical weathering and geologic carbon sequestration. These reactions, mainly dissolution/precipitation, will potentially alter formation properties including porosity and permeability. The rate and extent of these dissolution/precipitation reactions depends on the properties of the porous media such as mineral distribution, reactive surface area, flow rate, and the pore network structure. However, there is a large gap between observed field and laboratory or simulated reactions rates. This is in part due to the over/under estimation of parameters such as mineral accessible surface area, differences in reaction conditions chemical impurities and coupled reactions. Understanding the importance of these parameters is largely attributed to the heterogeneity of the samples particularly at the pore scale. This thesis explores two methods to improve understanding, and thus estimation, of reaction rates in porous media systems in the context of prospective geologic CO_2 storage in the Paluxy formation in Kemper County, MS (Project ECO_2S). First, additive manufacturing or 3D printing with custom reactive filaments is explored as a means to mimic the reactive properties of real rocks. Filaments are used to fabricate synthetic rocks based on the pore structure of a sandstone sample obtained from a 3D X-ray computed tomography (X-ray CT) image. The distribution and accessibility of the reactive minerals in the printed samples is then evaluated using 2D and 3D imaging. Second, direct numerical simulation is used to simulate three-dimensional flow and transport of ions at the pore scale using OpenFOAM in the pore-mesh of a sandstone sample obtained from a 3D X-

ray CT images. The Navier-Stokes and continuity equations are used for simulating flow and the transport of ions is simulated using the advection-diffusion equation. The simulation results, along with a new library to calculate rates of reaction and mesh motion as well as relaxation, will form the basis of a dynamic, multi-mineralic pore-scale reactive transport model.

Acknowledgments

I would like to thank my advisor Dr. Lauren E. Beckingham for providing me the opportunity to work with her and for all the advice and guidance throughout my time at Auburn. Thank you, my committee members Dr. Mark Barnett and Dr. Jose Goes Vasconcelos for their feedback and assistance in completing my thesis. I would like to thank my fellow group member: Chidera Iloejesi for bearing me by sharing the office, Fanqi Qin for all the fun time analyzing rock samples and Jeffrey Steinwinder for the tasty homemade burgers he cooked for us. I would also like to thank Haley Anderson and Shelby Wales for helping me with the chemical experiments in the lab. I will really miss going to AGU with Fanqi, Chidera and Jeffrey.

I would like to thank my parents, Shrikant V. Anjikar and Manisha S. Anjikar for always encouraging me to aim higher and supporting my education however possible. Thank you for believing in me and always supporting my decisions. I won't be standing where I am without their hard work and efforts.

To my Indian friends I made at Auburn, thank you for the wonderful time I had in these past two years. Thank you Vyom Parmar, I could not have asked for a better roommate than you. I could not have asked for better group of friends than Akshay Kadam, Aditya Mahajan, Priyanka Parab, Harsh Galia, Aditya Bachuwar, Shiva Prasad, Mehek Pyarali, Parinita Shetty and Hemendra Kumar. I am happy to have each of you in my life.

Lastly, I would like to thank Indian Student Association and Graduate Student Council committee members for the fun time organizing those wonderful events on campus and discussing issues related to graduate students.

Table of Contents

List of Tables

List of Figures

List of Abbreviations

ABS	Acrylonitrile Butadiene Styrene
AM	Additive Manufacturing
BSE	Back Scattered Electron
CFD	Computational Fluid Dynamics
DNS	Direct Numerical Simulation
FDM	Fused Deposition Modeling
HIPS	High Impact Polystyrene
PNM	Pore Network Modelling
SEM	Scanning Electron Microscopy
stl	Stereolithography
X-ray CT	X-ray Computed Tomography

Chapter 1: Introduction

Geochemical reactions in subsurface systems may result from natural processes such as weathering (Clark et al. 2018), microbiological activity (Teehera et al. 2018) or anthropogenic processes such as contaminant transport (Srivastava and Ramanathan 2018) and geologic carbon sequestration (Fuchs et al. 2019). These reactions can have a significant impact on the formation properties including porosity and permeability and may result in the development of preferential flow paths (Haug et al. 2011; Bacon et al. 2009; Cai et al. 2009). However, estimation of mineral reaction rates in porous media systems remains challenging and there are large discrepancies in the observed field scale rate of these reactions compared to those determined from laboratory and modelling studies. These discrepancies may be due to imprecision in the estimation of formation properties such as mineral accessible surface area (Beckingham et al. 2016) and mineral heterogeneities (Jung and Navarre-Sitchler 2018). There is a need for understanding these parameters and their corresponding impact on reaction rates specifically at the pore scale as these parameters depends on pore scale processes (Bourg et al. 2015). This thesis makes use of 3D printing and direct numerical simulation for improving the estimation of geochemical reaction rates in porous media in the context of geologic CO_2 sequestration using sandstone samples from a prospective CO_2 storage reservoir, the Paluxy formation in Kemper County, Mississippi.

1.1 Kemper county, MS site details

Kemper county is located in the central eastern region of Mississippi, U.S., sharing its border with Alabama. The Kemper county subsurface system consists of the northern limb of the Gulf of Mexico geosyncline and there are no major surface fault systems (Hughes 1958). Pashin et al. (2008) identified three cretaceous sandstone formations as potential storage reservoirs for geologic sequestration of CO_2: the Lower Tuscaloosa Group, the Washita-Fredericksburg interval and the Paluxy Formation. These sandstone formations, which are saline aquifers bounded with prominent caprocks, are located at depths of 3000 – 5000 feet, have porosities of 25 – 30% and have significant estimated storage capacity which makes them potential CO_2 storage formations (Esposito 2017). As part of the DOE CarbonSAFE supported Project ECO_2S, a pilot CO_2 injection site is being investigated close to the Integrated Gas Combined Cycle power plant in Kemper county. Figure 1.1 shows the location of this site while Figure 1.2 (Esposito 2017) shows the site map of this pilot project. The samples considered in this thesis are from the Paluxy formation extracted from well MPC 34-1, shown in Figure 1.2, from a depth of 1541 m.

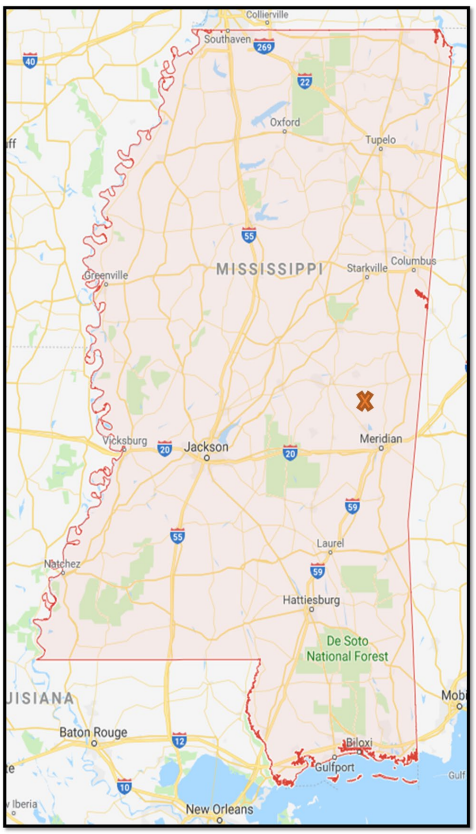

Figure 1.1: Location of Kemper pilot CO_2 injection site in Kemper county, Mississippi, U.S.

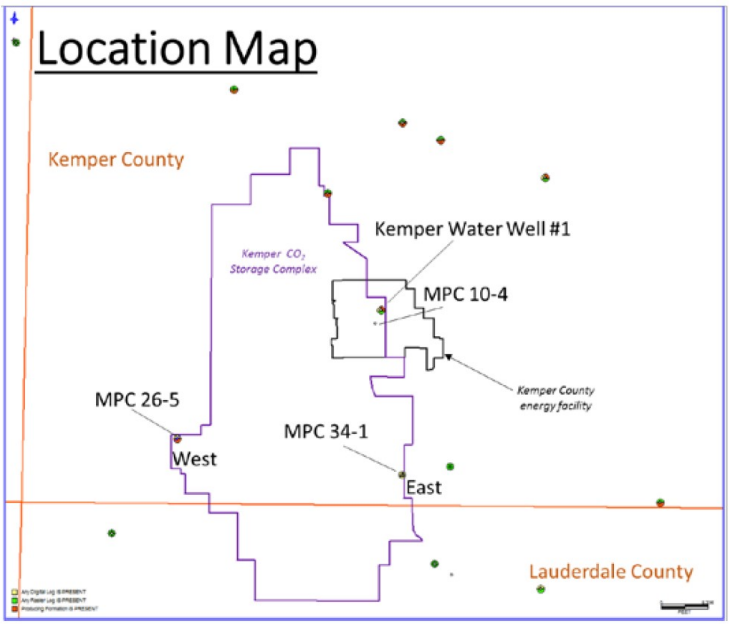

Figure 1.2: Site map of Project ECO_2S (Esposito 2017)

1.2 Feasibility study for the use of 3D printing to improve understanding of geochemical reaction rates in porous media.

3D printing has been widely used in various fields such as aerospace, biomedical, automotive (Ligon et al. 2017). In geosciences, it has been used for making microfluidics devices and sensors (Bhattacharjee et al. 2016; Rusling 2018), micromodel with pore triplet of constant depth and different widths of channel (Watson et al. 2018), printing temperature responsive hydrogels (Han et al. 2018) etc. Most previous studies on rock samples involved printing samples with polymers only (Kong et al. 2019; Ishutov et al. 2018). Here, the use of 3D printing to fabricate samples replicating natural porous samples with reactive minerals is explored. Novel custom filaments are made from mixture of high impact polystyrene (HIPS) pellets and calcite mixed in known weight percentages. Custom filaments are then used to 3D print rock samples based on real porous media structures obtained from 3D images of sandstone samples. Samples are printed using a fused deposition modelling (FDM) based 3D printer. The distribution and accessible surface area of calcite is evaluated using 2D Scanning Electron Microscopy (SEM) and 3D X-ray Computed Tomography (X-ray CT) and compared to the results for the sandstone sample determined in Qin and Beckingham (2019).

1.3 3D flow and transport simulation at pore scale using OpenFOAM

CO_2 injection into geologic storage formations can result in changes in porosity and permeability (Rathnaweera et al. 2016) as well as changes in chemical composition of the formation (Steefel et al. 2013; Molins et al. 2014). Mineral trapping of CO_2 usually happens over a time scale spanning over hundreds and thousands of years and running experiments over such long time periods can prove to be expensive and may not be feasible (Zhang et al. 2015). Numerical

modelling is a suitable method to overcome this issue and serve the need for understanding of pore scale feedback of flow and reactivity during mineral trapping (Bourg et al.2015). Here, the saline aquifer undergoing CO_2 injection is simulated to understand the distribution of Ca^{2+} and H^+ ions in the formation. Direct numerical simulations are developed and carried out in OpenFOAM (www.openfoam.org) to simulate fluid flow and the transport of ions using the Navier-Stokes, continuity and advection-diffusion equations. The simulation is carried out on a pore scale mesh generated from X-ray CT images of a rock sample from the Paluxy formation. This simulation will form the basis for developing the solver for simulating mineral dissolution/precipitation at the pore scale while calculating reaction rates and modify the physical mesh to reflect mineral growth and decomposition accordingly.

1.4 References

Bacon, Diana H., Bruce M. Sass, Mohit Bhargava, Joel Sminchak, and Neeraj Gupta. 2009. "Reactive Transport Modeling of CO_2 and SO_2 Injection into Deep Saline Formations and Their Effect on the Hydraulic Properties of Host Rocks." *Energy Procedia* 1 (1): 3283–90. https://doi.org/10.1016/J.EGYPRO.2009.02.114.

Beckingham, Lauren E., Elizabeth H. Mitnick, Carl I. Steefel, Shuo Zhang, Marco Voltolini, Alexander M. Swift, Li Yang, et al. 2016. "Evaluation of Mineral Reactive Surface Area Estimates for Prediction of Reactivity of a Multi-Mineral Sediment." *Geochimica et Cosmochimica Acta* 188 (September): 310–29. https://doi.org/10.1016/J.GCA.2016.05.040.

Bhattacharjee, Nirveek, Arturo Urrios, Shawn Kang, and Albert Folch. 2016. "The Upcoming 3D-Printing Revolution in Microfluidics." *Lab on a Chip* 16 (10): 1720–42. https://doi.org/10.1039/c6lc00163g.

Bourg, Ian C., Lauren E. Beckingham, and Donald J. DePaolo. 2015. "The Nanoscale Basis of CO_2 Trapping for Geologic Storage." *Environmental Science and Technology* 49 (17): 10265–84. https://doi.org/10.1021/acs.est.5b03003.

Cai, Rong, W. Brent Lindquist, Wooyong Um, and Keith W. Jones. 2009. "Tomographic Analysis of Reactive Flow Induced Pore Structure Changes in Column Experiments." *Advances in Water Resources* 32 (9): 1396–1403. https://doi.org/10.1016/J.ADVWATRES.2009.06.006.

Clark, Elyse V., W. Lee Daniels, Carl E. Zipper, and Kenneth Eriksson. 2018. "Mineralogical Influences on Water Quality from Weathering of Surface Coal Mine Spoils." *Applied Geochemistry* 91 (April): 97–106. https://doi.org/10.1016/J.APGEOCHEM.2018.02.001.

Fuchs, Samantha J., D. Nicholas Espinoza, Christina L. Lopano, Ange-Therese Akono, and

Charles J. Werth. 2019. “Geochemical and Geomechanical Alteration of Siliciclastic Reservoir Rock by Supercritical CO_2-Saturated Brine Formed during Geological Carbon Sequestration.” *International Journal of Greenhouse Gas Control* 88 (September): 251–60. https://doi.org/10.1016/J.IJGGC.2019.06.014.

Han, Daehoon, Zhaocheng Lu, Shawn A. Chester, and Howon Lee. 2018. “Micro 3D Printing of a Temperature-Responsive Hydrogel Using Projection Micro-Stereolithography.” *Scientific Reports* 8 (1): 1963. https://doi.org/10.1038/s41598-018-20385-2.

Haug, T. A., I. A. Munz, and R. A. Kleiv. 2011. “Importance of Dissolution and Precipitation Kinetics for Mineral Carbonation.” *Energy Procedia* 4: 5029–36. https://doi.org/10.1016/j.egypro.2011.02.475.

Hughes, Richard John. 1958. “Mississippi State Geological Survey: Kemper County Geology” 84.

Ishutov, Sergey, Franciszek J. Hasiuk, Dawn Jobe, and Susan Agar. 2018. “Using Resin-Based 3D Printing to Build Geometrically Accurate Proxies of Porous Sedimentary Rocks.” *Groundwater* 56 (3): 482–90. https://doi.org/10.1111/gwat.12601.

Jung, Heewon, and Alexis Navarre-Sitchler. 2018. “Scale Effect on the Time Dependence of Mineral Dissolution Rates in Physically Heterogeneous Porous Media.” *Geochimica et Cosmochimica Acta* 234 (August): 70–83. https://doi.org/10.1016/J.GCA.2018.05.009.

Kong, Lingyun, Mehdi Ostadhassan, Xiaodong Hou, Michael Mann, and Chunxiao Li. 2019. “Microstructure Characteristics and Fractal Analysis of 3D-Printed Sandstone Using Micro-CT and SEM-EDS.” *Journal of Petroleum Science and Engineering* 175 (April): 1039–48. https://doi.org/10.1016/J.PETROL.2019.01.050.

Landrot, Gautier, Jonathan B. Ajo-Franklin, Li Yang, Stefano Cabrini, and Carl I. Steefel. 2012.

"Measurement of Accessible Reactive Surface Area in a Sandstone, with Application to CO_2 Mineralization." *Chemical Geology* 318–319: 113–25. https://doi.org/10.1016/j.chemgeo.2012.05.010.

Ligon, Samuel Clark, Robert Liska, Jürgen Stampfl, Matthias Gurr, and Rolf Mülhaupt. 2017. "Polymers for 3D Printing and Customized Additive Manufacturing." *Chemical Reviews* 117 (15): 10212–90. https://doi.org/10.1021/acs.chemrev.7b00074.

Liteanu, Emilia, and Christopher J. Spiers. 2009. "Influence of Pore Fluid Salt Content on Compaction Creep of Calcite Aggregates in the Presence of Supercritical CO_2." *Chemical Geology* 265 (1–2): 134–47. https://doi.org/10.1016/J.CHEMGEO.2008.12.010.

Molins, Sergi, David Trebotich, Li Yang, Jonathan B. Ajo-Franklin, Terry J. Ligocki, Chaopeng Shen, and Carl I. Steefel. 2014. "Pore-Scale Controls on Calcite Dissolution Rates from Flow-through Laboratory and Numerical Experiments." *Environmental Science and Technology* 48 (13): 7453–60. https://doi.org/10.1021/es5013438.

Pashin, Jack C, Denise J Hills, David C Kopaska-merkel, and Marcella R Mcintyre. 2008. "Geological Evaluation of the Potential for CO_2 Sequestration in Kemper County , Mississippi Prepared By."

Qin, Fanqi, and Lauren E. Beckingham. 2019. "Impact of Image Resolution on Quantification of Mineral Abundances and Accessible Surface Areas." *Chemical Geology* 523 (September): 31–41. https://doi.org/10.1016/j.chemgeo.2019.06.004.

Rathnaweera, T. D., P. G. Ranjith, and M. S. A. Perera. 2016. "Experimental Investigation of Geochemical and Mineralogical Effects of CO_2 Sequestration on Flow Characteristics of Reservoir Rock in Deep Saline Aquifers." *Scientific Reports* 6 (1): 19362. https://doi.org/10.1038/srep19362.

Rusling, James F. 2018. “Developing Microfluidic Sensing Devices Using 3D Printing.” https://doi.org/10.1021/acssensors.8b00079.

Srivastava, Sunil Kumar, and AL Ramanathan. 2018. “Assessment of Landfills Vulnerability on the Groundwater Quality Located near Floodplain of the Perennial River and Simulation of Contaminant Transport.” *Modeling Earth Systems and Environment* 4 (2): 729–52. https://doi.org/10.1007/s40808-018-0464-7.

Steefel, Carl I, Sergi Molins, and David Trebotich. 2013. “Pore Scale Processes Associated with Subsurface CO_2 Injection and Sequestration.” *Reviews in Mineralogy & Geochemistry* 77: 259–303. https://doi.org/10.2138/rmg.2013.77.8.

Teehera, Kimberly B, Sean P Jungbluth, Bogdan P Onac, Tayro E Acosta-Maeda, Eric Hellebrand, Anupam K Misra, Andreas Pflitsch, et al. 2018. “Cryogenic Minerals in Hawaiian Lava Tubes: A Geochemical and Microbiological Exploration.” *Geomicrobiology Journal* 35 (3): 227–41. https://doi.org/10.1080/01490451.2017.1362079.

Waldmann, Svenja, Andreas Busch, Kees van Ojik, and Reinhard Gaupp. 2014. “Importance of Mineral Surface Areas in Rotliegend Sandstones for Modeling CO_2–Water–Rock Interactions.” *Chemical Geology* 378–379 (June): 89–109. https://doi.org/10.1016/J.CHEMGEO.2014.03.014.

Watson, Francesca, Julien Maes, Sebastian Geiger, Eric Mackay, Mike Singleton, Thomas Mcgravie, Terry Anouilh, et al. 2018. “Comparison of Flow and Transport Experiments on 3D Printed Micromodels with Direct Numerical Simulations.” *Transport in Porous Media*. https://doi.org/10.1007/s11242-018-1136-9.

Zhang, Liwei, Yee Soong, Robert Dilmore, and Christina Lopano. 2015. “Numerical Simulation of Porosity and Permeability Evolution of Mount Simon Sandstone under Geological

Carbon Sequestration Conditions." *Chemical Geology* 403: 1–12. https://doi.org/10.1016/j.chemgeo.2015.03.014.

Zhang, X, J Salemans, C J Peach, and C J Spiers. 2002. "Compaction Experiments on Wet Calcite Powder at Room Temperature: Evidence for Operation of Intergranular Pressure Solution." Edited by S de Meer, M R Drury, J H P de Bresser, and G M Pennock. *Deformation Mechanisms, Rheology and Tectonics: Current Status and Future Perspectives*. Geological Society of London. https://doi.org/10.1144/GSL.SP.2001.200.01.02.

Chapter 2: Feasibility of 3D printing to improve understanding of geochemical reaction rates in porous media.

Ishan Anjikar[1], Lauren E. Beckingham[1]*
[1]***Department of Civil Engineering, Auburn University, Auburn, AL 36849***
leb@auburn.edu
Manuscript in preparation.

2.1 Abstract

The rate and extent of geochemical reactions in subsurface systems is not well understood and there are large discrepancies between field observed rates and those simulated or experimentally observed. Laboratory experiments estimating reaction rates typically use disaggregated pure mineral samples which are unable to reflect conditions in natural porous media. In addition, the natural heterogeneities of samples make it difficult to isolate the impacts of variations in parameters. This work explores the use of 3D printing to fabricate synthetic rock samples with reactive properties mimicking those of natural porous media samples. Here, X-ray CT images of a sandstone from the Paluxy formation were used to generate a porous media mesh. This mesh was used as the basis for 3D printing of synthetic samples replicating the pore network structure of the Paluxy formation. Novel, reactive filaments for 3D printing were constructed from mixtures of high impact polystyrene and calcite mixed in known weight fractions of 5% to 20%. Synthetic rock samples were then printed using these novel filaments with a fused deposition modelling based 3D printer. The distribution and accessible calcite surface area of printed samples were evaluated using scanning electron microscopy and X-ray CT imaging.

These properties were compared to values for the real rock sample. Synthetic rock samples had accessible calcite surface area comparable to real samples though the fraction of calcite present on surface was very less.

2.2 Introduction

Contaminant transport (Essaid et al. 2015; Goh and Lim 2004; Sandhu et al. 2018), microbiological reactions (Hunter et al. 1998; Jin and Bethke 2005), acid injection for enhanced oil recovery (Zhu et al. 2018) or CO_2 injection into deep saline aquifers (Bachu et al. 1994; De Silva et al. 2015; Deng et al. 2015; Black et al. 2015; Xiong et al. 2018; Beckingham et al. 2017), can result in geochemical reactions in subsurface systems. Reactions, mainly mineral dissolution and precipitation reactions, can have a significant impact on the chemical and physical properties of the system, altering formation fluid chemistry and porosity and permeability (Ross et al. 1982; Shiraki and Dunn 2000; Yu et al. 2012; Beckingham et al. 2013; Rathnaweera et al. 2016). Even though there is good understanding of the changes in porosity due to dissolution/precipitation reactions (Deng et al. 2015; Zou et al. 2018), there are large imprecisions in estimation of reaction rates for these systems (Bachu et al. 2007; Bourg et al. 2015; Beckingham et al. 2016; Wen and Li 2018; Jung and Navarre-Sitchler 2018). In porous media systems, the rate of reaction has been observed to depend on the pore structure (Pereira Nunes et al. 2016), accessible mineral surface area (Beckingham et al. 2017), flow paths and concentration gradient (Molins et al. 2012). However, mineral dissolution rates have been typically estimated from laboratory experiments that use disaggregated pure mineral phases (X. Zhang et al. 2002; Liteanu and Spiers 2009) are fundamentally unable to reflect the reaction conditions in real porous media samples. Laboratory experiments on physical core or rock

samples often lead to the sample being disturbed or destroyed, thus ceasing its use for another experiment (Josh et al. 2012; Vishal et al. 2015; Bultreys et al. 2016; Ameloot et al. 2016; Elhami et al. 2016). Another sample from the same formation can be used, which has similar chemical properties, but no two samples have identical pore structures (Al-Khulaifi et al. 2018; Liu et al. 2017).

Additive manufacturing (AM) or 3D printing has emerged as a powerful tool to create porous media samples with controlled features and even identical pore structures (Ishutov et al. 2018; Kong et al. 2019). AM is the process of joining materials to make parts from 3D model data (ASTM International 2015), usually layer upon layer as in Fused Deposition Modeling (FDM) (Guo and Leu 2013). 3D printing has been widely used in aerospace, automotive, biomedical, and art fields (Ligon et al. 2017) and has been recently used for fabricating microfluidic devices (Mcdonald and Whitesides 2002; Bhattacharjee et al. 2016; Rusling 2018, Watson et al. 2018) and bench scale flow through reactors for water treatment (Loeb et al. 2019). The potential use of 3D printing for fabricating geological materials for use in lab experiments has been considered for undisturbed soil samples (Bacher et al. 2015; Dal Ferro and Morari 2015; Otten et al. 2012), sandstones (Ishutov et al. 2015; Kong et al. 2019), and sedimentary rocks (Ishutov et al. 2018). All these studies were focused on replicating the pore network of natural samples. The applicability of 3D printed samples to replicate flow properties, namely bulk porosity and permeability (Head and Vanorio 2016) and rock mechanics (Jiang et al. 2016; Jiang and Zhao 2015; Hodder et al. 2018) has also been investigated. Although the use of 3D printing is growing in geoscience applications, the feasibility of 3D printing to be utilized in geochemically reactive systems has never been considered.

This work explores the utility of FDM technology for 3D printing synthetic porous media samples with reactive properties mimicking natural samples to enhance understanding of geochemical reactions in porous media. Using this approach, samples with identical pore structures could be fabricated and used in replicate experiments devised to isolate the role of individual parameters on mineral reactions and reaction rates in porous media, eliminating experimental uncertainties that exist even on replicate samples from the same location. Here, novel calcite-containing filament with varying weight percentages of calcite are fabricated. Synthetic rock samples are then printed using these custom filaments based on the pore structure of sandstone sample. The distribution and accessible surface area of calcite in the 3D printed samples is then computed from 2D and 3D images of the printed samples.

2.3 Methods

2.3.1 Filament preparation

2.3.1.1 Acid resistance testing

In environmental systems, acidic conditions are often drivers for geochemical reactions, e.g. acid mine drainage, acid rain, acid injection for enhanced oil recovery, and geologic carbon sequestration. In particular, this work seeks to utilize 3D printing to evaluate reactions in the context of CO_2 injection at the Kemper pilot CO_2 injection site in Kemper County, MS (Project ECO_2S). As such, potential filament base materials, which has printing temperature lower than the temperature at which Iceland spar calcite would completely lose crystallinity, were tested for changes in morphology and weight after interacting with acid. Batch scale acid resistance tests were developed and carried out with 10 mm printed cubes of High Impact Polystyrene (HIPS) and Acrylonitrile Butadiene Styrene (ABS). Cubes with 100% infill were 3D printed using a

Lulbotz Taz4 3D printer using 2.85 mm filament. The cubes were printed using 0.5 mm nozzle with nozzle temperature of 240°C and bed temperature of 110°C. Samples were printed with 100% infill, 50% fan speed and a layer height of 0.25 mm. The initial weight of the cubes was noted before the experiment. Cubes were then placed in 80 mL of acidic solution with an initial pH of 3.5 in a beaker at room temperature. The acidic solution was made by diluting 1M hydrochloric acid with deionized water. Each cube was placed in a separate beaker and the beaker was covered with aluminum foil to avoid interaction with air. During the experiment, cubes were kept in the solution for 1 hr, 2 hrs, 4 hrs and 24 hrs and the pH of the solution tracked. A control sample was also prepared and consisted of just the acidic solution in a beaker. After the specified time, the cube was removed from the beaker, washed with deionized water, and dried for 2 weeks at room temperature before measuring the cube weight. Change in weight was calculated using equation 2.1.

$$Change\ in\ weight(\%) = \left(\frac{Final\ weight - Initial\ Weight}{Intial\ weight}\right) * 100 \qquad (2.1)$$

Additional long-term experiments were carried out, reusing the cubes used in the short term experiments. In these experiments, cubes were kept in the acidic solution for 3 days, 5 days and 7 days. At the specified time, cubes were removed from acid, dried, and weighed. Based on the experiment, HIPS was found to be more suitable material for making 3D printed rocks and utilized in preparation of the novel reactive filament. The detailed results are discussed in Section 3.1.

2.3.1.2 Reactive filament construction

Reactive filament was made by mixing known weights of powdered Iceland spar calcite and HIPS 8 MELT 2 IZOD pellets. Iceland spar calcite has been used in many calcite dissolution

experiments (Peng et al. 2015; Plummer et al. 1976; Molins et al. 2014) because of its purity. Here, calcite crystals were crushed, powdered and segregated into 63-90 μm size particles using ASTM sieves no. 170 and 230. HIPS pellets and segregated calcite powder were mixed together to obtain a batch with calcite weight fraction of 5%, 10%, 15% and 20%. Each batch of pellets and calcite powder mixture was loaded into the hopper of Filabot EX2 filament extruder and extruded into filament at a temperature of 210°C. The filament extrusion rate was controlled to achieve a filament thickness of approximately 2.6 mm.

2.3.2 Mesh generation from 3D X-ray CT image

A sandstone sample from the Paluxy formation in Kemper county, Mississippi considered in Qin and Beckingham (2019) was selected here as the basis for 3D printing. This sample was extracted from well MPC 34-1 from a depth of 1541 m. 3D X-ray CT images collected on a 0.5 cm x 0.5 cm x 1 cm cuboid at a resolution of 6.62 microns and segmented in Qin and Beckingham (2019) were utilized here. The original X-ray CT image stack, with porosity of 0.26, was subsampled here to extract a 100 x 100 x 100 voxel cube. A wavefront (.obj) mesh for the grains was then generated with ImageJ. The mesh was then processed in Blender to remove unconnected grains. The resulting mesh was then enlarged by twenty times to ensure that all the pores could be reproduced properly when printing and exported as a stereolithography (.stl) file.

2.3.3 3D printing of rock samples

To prepare for 3D printing, the mesh files were first converted into a 3D printer supported format, gcode, using Cura v3.2.27. Before deciding on the settings to be used for 3D printing the samples, various printing conditions were tested. Samples were printed using a Lulbotz Taz4

printer with bed temperature set at 100°C, 110°C and 120°C, nozzle temperature at 230°C and 240°C, layer thickness and height of 0.2 mm, 0.25 mm and 0.3 mm and 40%, 50%, 60% and 100% fan speed with an objective of printing samples with low internal porosity and avoiding nozzle clogging.

Based on visual inspection of the samples printed with different printing conditions, samples were finally printed with nozzle temperature of 240°C and bed temperature of 110°C from 0.5 mm nozzle with 100% infill, 50% fan speed, and a layer thickness and height of 0.25 mm. Three sample sets were printed using three different filaments, those containing 5%, 10% and 15% calcite. Identical printing conditions were used for printing with each filament. Each sample set consisted of two replicate cubes where one cube was used for subsequent Scanning Electron Microscopy (SEM) analysis and the other was used for X-ray CT analysis.

2.3.4 Image analysis of 3D printed samples

2.3.4.1 2D imaging analysis

3D printed samples were imaged using 2D scanning electron microscopy (SEM) operated in backscatter electron (BSE) mode using a ZEISS EVO 50VP Scanning Electron Microscope at Auburn University. Before imaging, samples were coated with carbon using EMS 550X Sputter Coating Device. A SEM beam intensity of 20 kV was used, and images were collected at a resolution of 3 microns. The calcite distribution in each sample was inspected by segmenting the images into pores, calcite and HIPS. The fraction of each phase was determined by counting the segmented pixels of each phase and dividing by total number of pixels.

2.3.4.2 3D imaging analysis

3D X-ray CT images were collected for the 5% and 15% calcite containing samples using a NANO-CT-GE V|TOME|X M 240 at the Research Service Center, Herbert Wertheim College of Engineering, University of Florida. Images were captured at a voxel resolution of 11 microns. Collected images were cropped to obtain a 900 x 900 x 900 voxel cube and segmented into pores, HIPS and calcite using Matlab. Calcite voxels were further differentiated between those present on the surface i.e. in contact with the pores and those present inside the sample. The total porosity was calculated by counting the number of pore voxels in the segmented image and dividing by the total number of voxels in the cube. The connected porosity was then determined using a marching cube and burning algorithm modified from Landrot et al. (2012) and Beckingham et al. (2017). The accessible calcite surface area was then calculated by first identifying calcite and HIPS voxels in contact with pore voxels. A mesh was then applied to the pore-bordering surface of calcite and HIPS voxels and the surface area of the mesh was calculated by adding the area of individual faces on the mesh. The calcite surface area was calculated by multiplying the mesh surface area by the proportion of pore-bordering voxels corresponding to calcite. The total mass of calcite present in the sample was then calculated by multiplying total volume of calcite voxels by the bulk density of Iceland spar calcite, 2.71g/cm^3 (Lambkin et al. 2011). The normalized accessible calcite surface area then was determined by dividing the calcite surface area by the mass of calcite present in sample.

2.4 Results and Discussion

2.4.1 Filament preparation

2.4.1.1 Acid resistance testing

Figure 2.1 shows the HIPS and ABS cubes printed for the acid resistance test. The change in sample weight and the evolution of pH for the acid resistance test of HIPS and ABS cubes are shown in Figure 2.2 and 2.3. As evident from Figure 2.2, overall variations in pH were small, within ±0.3 of the initial value, and there was a larger change in pH for ABS as compared to HIPS. Also, the pH for the HIPS samples was closer to that of control values. It can be observed from Figure 2.3 that the weight changes were not significant in either case, ranging from 0.007% to 0.204%. It was observed that the weight increased for both the samples due to trapping of the solution in the cubes even after drying. Larger weight changes were observed at short times as compared to long times as some of the loosely connected parts of the printed sample were separated during the experiment resulting in more solution entering the cube, thus higher weight change. The weight change in long times was lower as some parts of these cubes may have swollen and blocked some areas where solution was trapped previously.

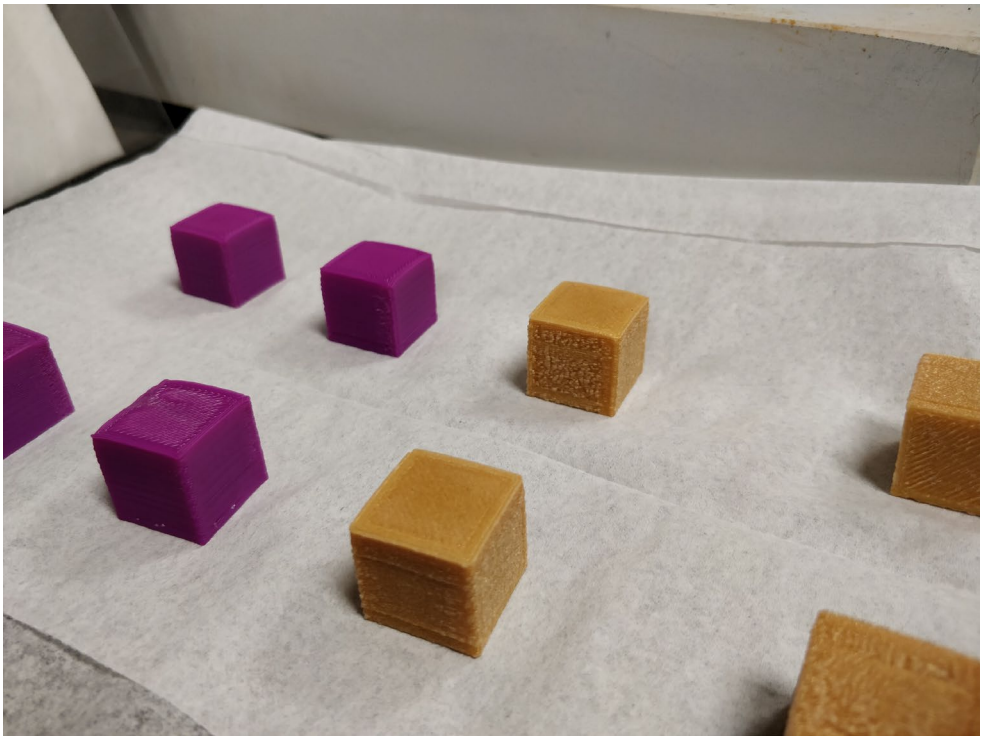

Figure 2.1: HIPS (purple) and ABS (yellow) cubes printed for acid resistance test.

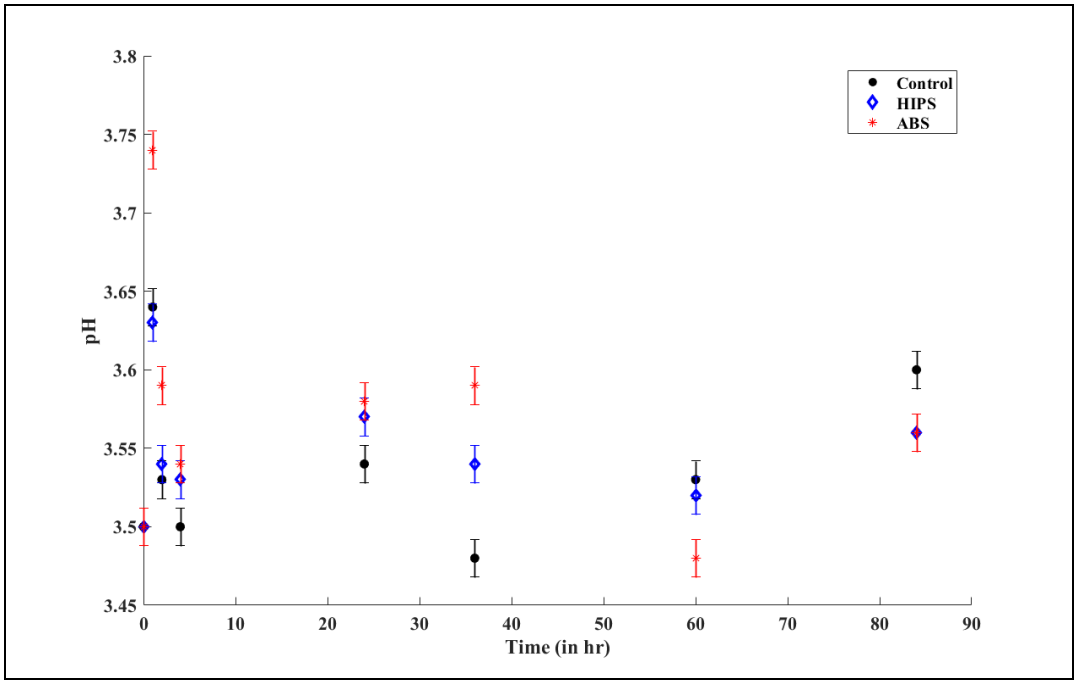

Figure 2.2: pH change during acid resistance test

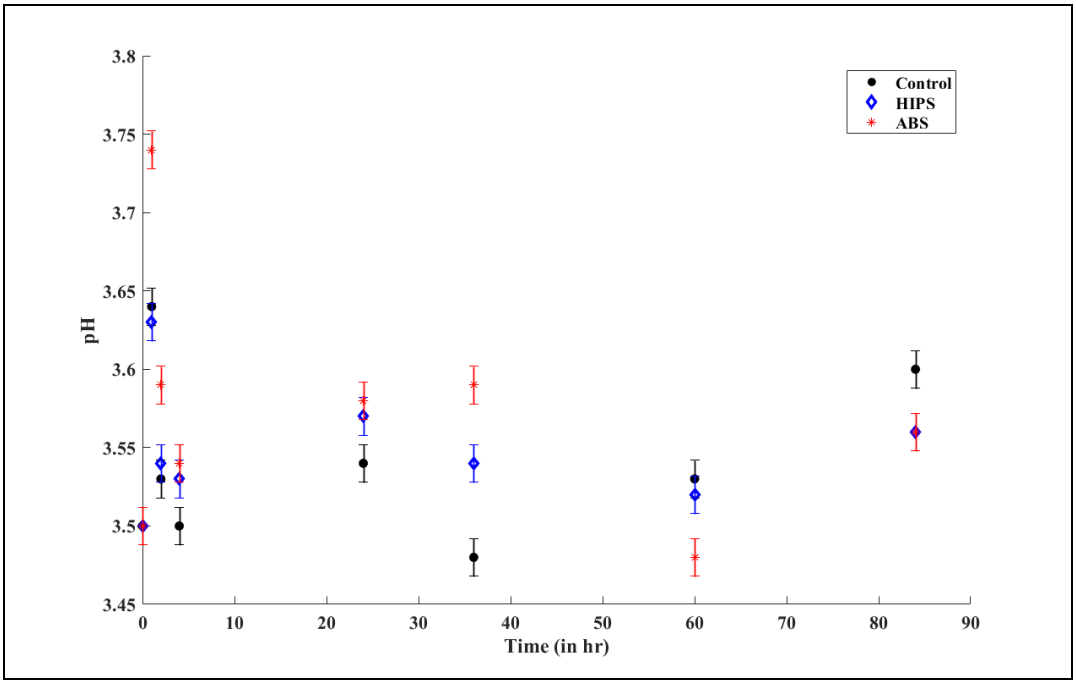

Figure 2.3: Weight change during acid resistance test

2.4.1.2 Reactive filament construction

Figure 2.4 shows the images of four filaments prepared for 3D printing as viewed under an optical microscope. Filament extrusion was highly influenced by the amount of calcite mixed with HIPS. As the amount of calcite increased in the mixture, maintaining desired filament thickness and uniformity became difficult. In addition, an increase in filament stiffness was observed with increasing calcite content. Maintaining uniform composition of the filament was also challenging and calcite agglomeration was prevalent in the filament made with 20% calcite. The 20% filament also had bubbles on its surface and significant calcite agglomeration, thus it was not of acceptable quality to be used for 3D printing as the section of filament with agglomerated calcite particles would result in clogging on nozzle and the surface defects in the filament would result in printing defects in the sample. Deviations in desired thickness where much less apparent in filaments with 5%, 10% and 15% calcite and they also maintained

flexibility. However, deviations from the desired thickness of 2.6 mm were apparent sporadically in the 15% calcite filament. As such, the 5%, 10%, and 15% calcite filaments were selected for 3D printing where a section of the 15% calcite filament that maintained the desired thickness was isolated from the problematic areas and used for 3D printing.

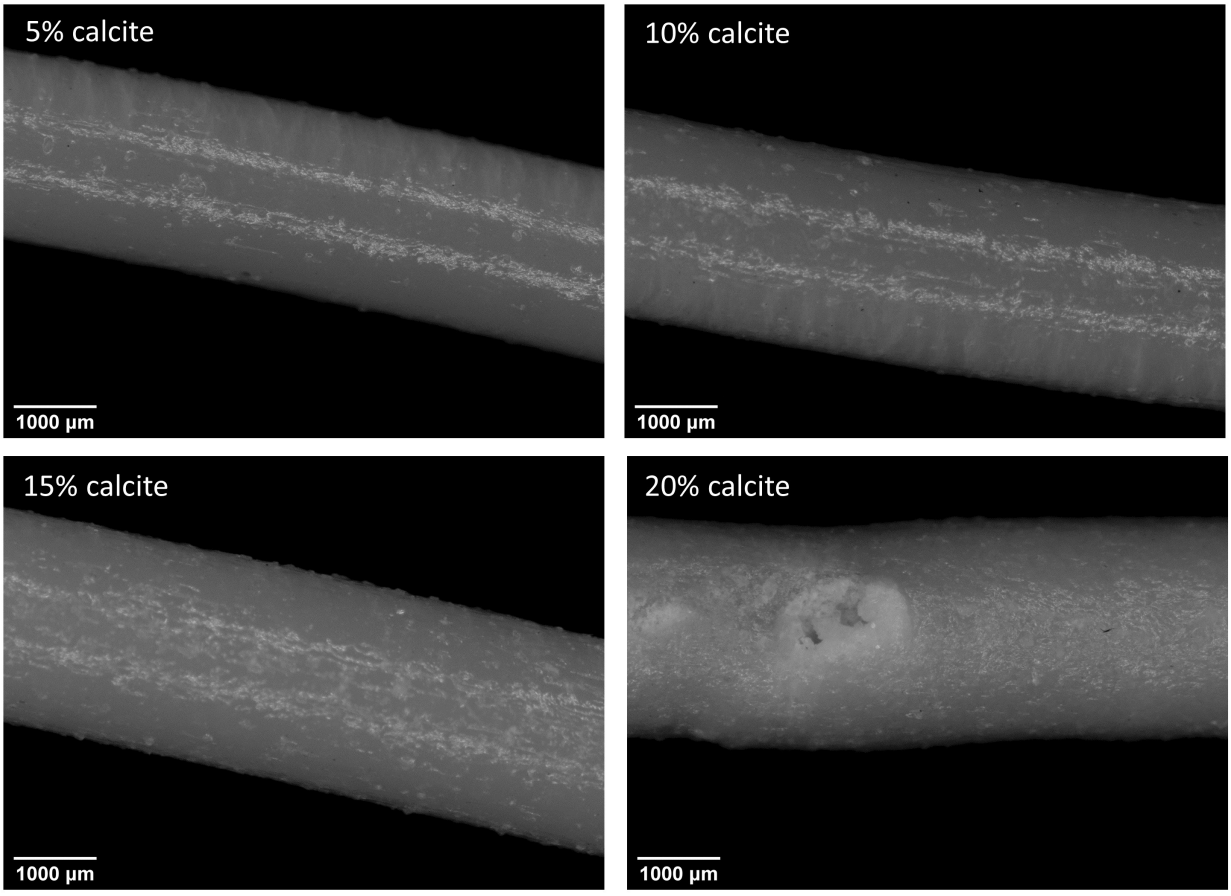

Figure 2.4: Images of custom filament under optical microscope.

2.4.2 Mesh generation from 3D X-ray CT image

The thresholded 3D X-ray CT image of the Paluxy sandstone to be utilized as the basis for mesh generation is shown in Figure 2.5 (a). The resulting mesh generated from the X-ray CT image after image processing in ImageJ and mesh processing in Blender is shown in Figure 2.5 (b). The

mesh has a porosity of 0.2917 while the porosity of the X-ray CT sub-sample is 0.2652, which is similar to the porosity of 0.26 of the original sample. The higher porosity in the mesh is a result of removing unconnected grains that cannot be printed with 3D printing.

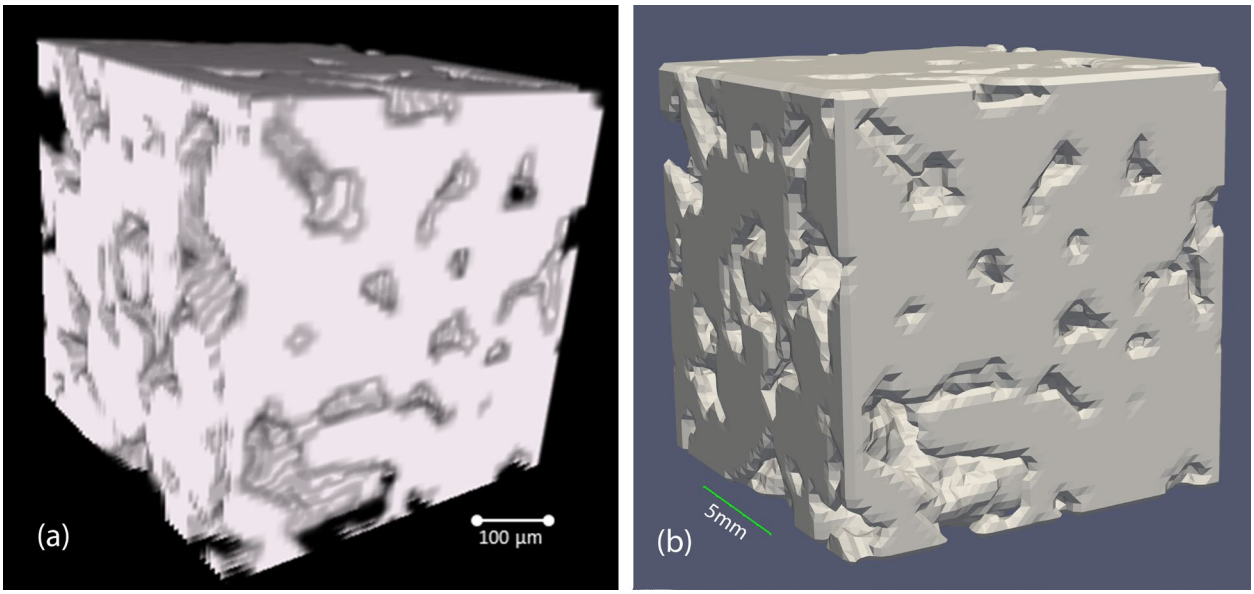

Figure 2.5: (a) Thresholded 3D X-ray CT image with grains in white, (b) 3D stereolithography mesh generated form X-ray CT images corresponding to grains.

2.4.3 3D printing of rock samples

Figure 2.6 shows the 3D printed samples using the 5%, 10% and 15% calcite filament. Layers in the 5% calcite sample have better overlap and transition as there are no gaps between printed layers. Also, there were no unintended gaps while printing in the same layer in 5% sample. Thus, print quality is better in the 5% calcite sample as compared to other two samples.

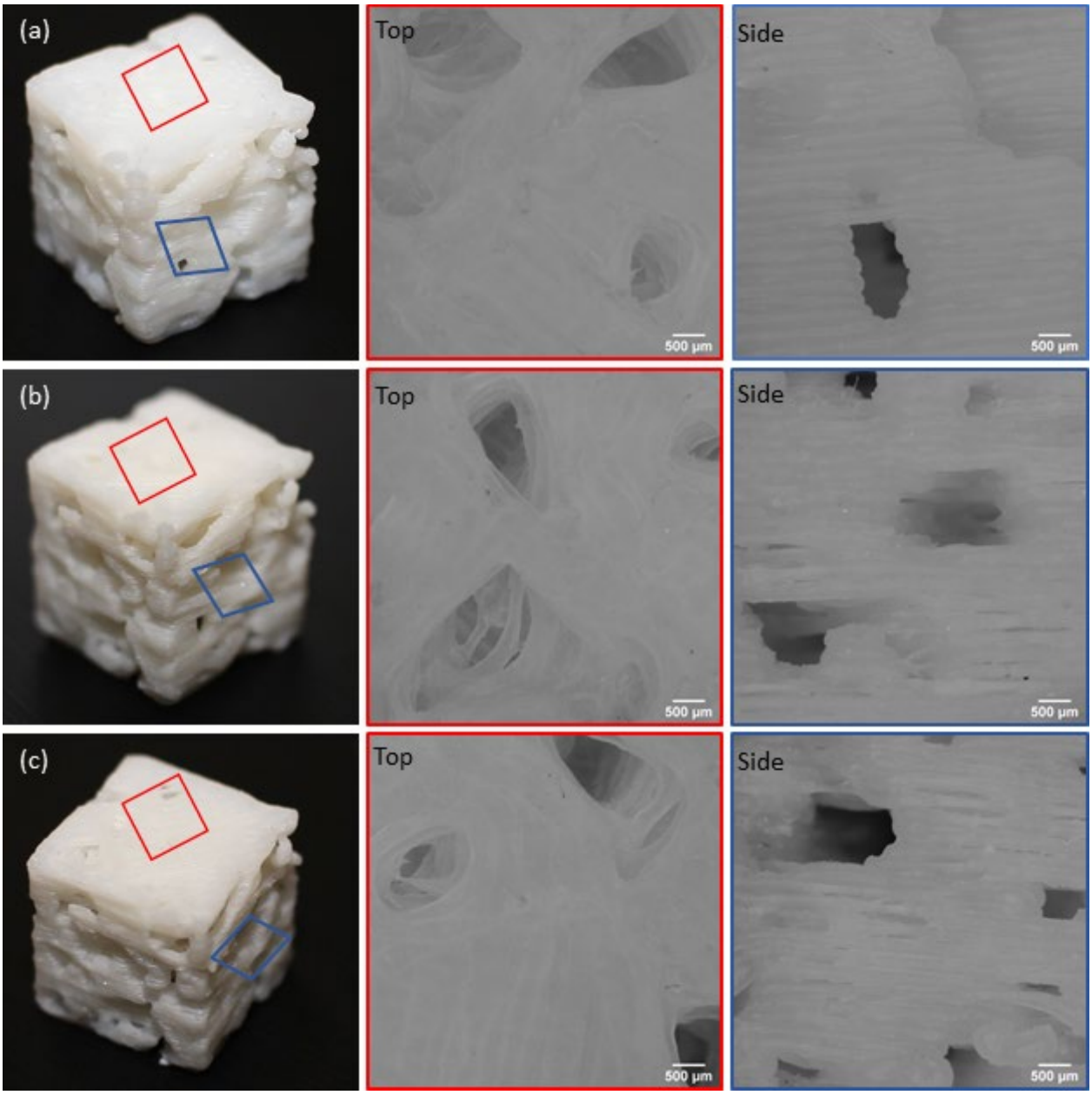

Figure 2.6: Images of 3D printed samples (a) 5%, (b) 10%, and (c) 15% and the corresponding top and side images taken under microscope. The location of red and blue box shows the approximate location of the microscopic images of top and side on the right.

2.4.4 Imaging analysis of 3D printed samples

2.4.4.1 SEM analysis

The SEM BSE images of the 5%, 10% and 15% calcite containing samples are shown in Figure 2.7. It should be noted that the images are not from the same section of the three cubes. The darker areas in these images correspond to pores and the brightest pixels corresponds to calcite. The remaining areas represent the HIPS. Table 2.1 shows the fraction of each component in the three images obtained by pixel counting. The porosity of the samples varies from 8.05% to a maximum of 14.62% for the 10% sample. It was also evident from the SEM images that the internal porosity increased in 10% and 15% sample due to improper overlap between layers though it was not visible with naked eye. An increase in calcite is clear for the 10% and 15% sample compared to the 5% sample. However, the 10% and 15% samples contain a similar percentage of calcite in the SEM images which may be a result of non-uniform distribution of calcite in the filament used for printing. Thus, to analyze samples with more variability in the calcite composition the 5% and 15% calcite samples were selected for X-ray CT analysis.

Table 2.1: Percentages of different components in SEM images of the three 3D printed samples.

Sample	Pores (%)	HIPS (%)	Calcite (%)
5%	8.03	90.10	1.87
10%	14.62	81.02	4.36
15%	10.20	85.48	4.32

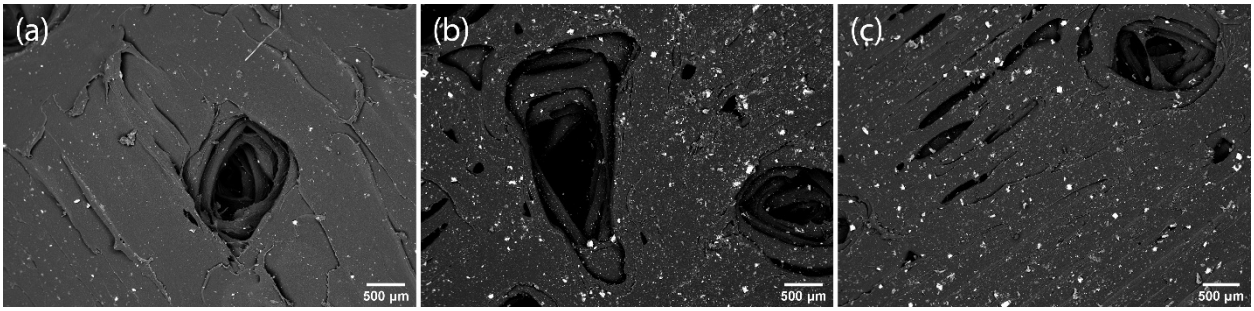

Figure 2.7: SEM images for 3D printed samples with (a) 5% calcite, (b) 10% calcite, (c) 15% calcite. Black areas correspond to pores, white areas to calcite and the remaining region is HIPS.

2.4.4.2 X-ray CT analysis

X-ray CT images of the 5% and 15% calcite sample are shown in Figure 2.8. Brighter pixels represent calcite, grey areas represent HIPS and the black region represent pores. As evident in the X-ray CT images, the amount of calcite is much higher in the 15% sample as compared to 5% sample. Table 2.2 shows the percentages of each component computed by counting voxels in the segmented image. The porosity of the 5% sample is 0.2812 and that of the 15% sample is 0.3371. The porosity of the 5% sample is less than the 15% sample and closer to that of the original sample 0.26. This increase in porosity is due to an increase in unintended internal porosity in the 15% sample which was also observed in the SEM images of the sample. The amount of calcite in the 15% sample is approximately double that of the 5% sample and for both samples, there is more than 50% reduction in the amount of calcite amount in 3D printed sample as compared to what was used while fabricating filament. This may have occurred due to the non-uniform distribution of calcite in the filament.

Table 2.2: Percentages of different components in sub-sample taken from X-ray CT images of the 3D printed samples

Sample	Pores (%)	HIPS (%)	Calcite (%)
5% sample	28.12	69.77	2.11
15% sample	33.71	62.09	4.20

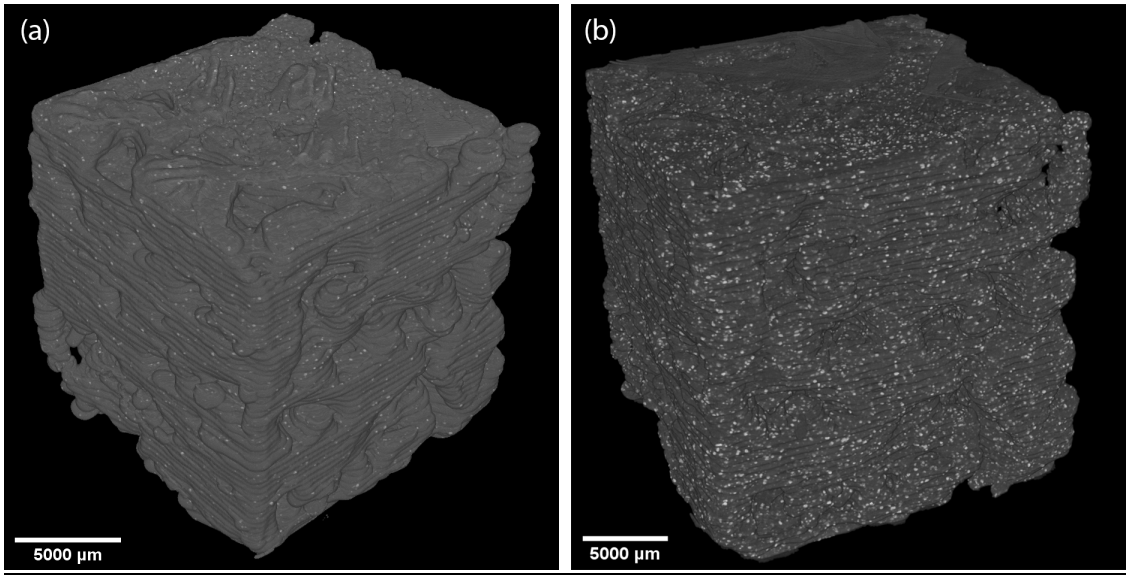

Figure 2.8: X-ray CT images of 3D printed samples fabricated with filament containing (a) 5% calcite and (b) 15% calcite.

Table 2.3 shows the distribution of calcite in the 5% and 15% sample. 5% sample has 0.4% calcite on the surface, while the 15% sample has 0.17% calcite on the surface. The percentage of calcite present on the surface is less than 0.5% in both the sample, but it is lower in case of 15% sample as compared to 5% sample.

Table 2.3: Distribution of calcite in the 3D printed samples

Sample	Calcite inside sample (%)	Calcite on the surface (%)
5% sample	99.60	0.40
15% sample	99.83	0.17

Table 2.4 shows the total porosity, connected porosity, total accessible surface area, accessible calcite surface area and normalized accessible calcite surface area calculated from X-ray CT images of two samples. The connected porosity of the 5% sample and 15% samples are 0.2812 and 0.3370 respectively. There is not much decrease in connected porosity as compared to total porosity which would indicate that the unintended internal pore space is also connected to the actual pore space in 15% sample. One possible reason for no reduction in connected porosity in both the samples can be the small size of the samples, where all the pores are connected. The total accessible surface area of the 5% and 15% samples are 28.41×10^{-4} m^2 and 43.11×10^{-4} m^2. The increase in total accessible surface area is due to the increased connected porosity in the 15% sample. The accessible calcite surface area for the 5% and 15% samples is 8.03×10^{-6} m^2 and 6.80×10^{-6} m^2 respectively. Although the 15% sample has more porosity and almost 50% more total accessible surface area as compared to 5% sample, the accessible calcite surface area is higher in the 5% sample. This is due to the higher amount of calcite present on the surface in case of 5% sample as compared to 15% sample. The normalized accessible calcite area of the 5% and 15% sample are 1.45×10^{-4} m^2/g and 0.62×10^{-4} m^2/g respectively. The normalized accessible calcite surface area calculated here is order of magnitude lower than those calculated in Qin and Beckingham (2019) where the accessible calcite area was around 3×10^{-3} m^2/g and composition of calcite was almost 9% as opposed to 2.11% and 4.20% calcite in 5% and 15% sample. But these values are higher as compared to 2.14×10^{-5} m^2/g reported in Beckingham et al. (2017) where the sample contained 0.03% calcite by volume. Lower mineral accessible surface area in their sample was due to the presence of clay coatings on the mineral grains, which reduces the mineral accessibility.

Table 2.4: Sample properties calculated from the X-ray CT images of 5% and 15% sample are shown here.

Sample property	5% sample	15% sample
Total Porosity	0.2812	0.3371
Connected Porosity	0.2812	0.3370
Total accessible surface area	28.41×10^{-4} m^2	43.11×10^{-4} m^2
Accessible calcite surface area	8.03×10^{-6} m^2	6.80×10^{-6} m^2
Amount of calcite	5.55×10^{-2} g	11.06×10^{-2} g
Normalized accessible calcite surface area	1.45×10^{-4} m^2/g	0.62×10^{-4} m^2/g

2.5 Conclusion

3D printing rock structures with geochemically reactive minerals was explored here as a means to replicate natural porous samples. Polymers suitable for 3D printing were tested for their compatibility to be used in acidic conditions typically found in environmental systems with geochemical reactions. While neither polymer test exhibited significant signs of degradation, HIPS was found to be more resilient as compared to ABS during acid resistance testing and thus suitable for fabricating samples to be utilized in acidic laboratory experiments.

Custom filaments were made with mixtures of calcite and HIPS with different weight fractions. This work observed that the amount of calcite that can used with HIPS was between 15 - 20%. Similar, restrictions have been observed by Hodder et al. (2018) with respect to the amount of binder material that can be present in the sample. As the amount of calcite increased in the filament, maintaining uniformity in the calcite distribution and filament thickness was increasingly challenging. This resulted in variations in calcite content in the printed samples as compared to the anticipated calcite content where samples contained less than 50% of the calcite used in the bulk filament. Printing samples with filaments containing higher amounts of calcite

was additionally difficult and resulted in increased defects. Samples printed using filament with 15% calcite had unintended internal porosity in the printed samples.

Calcite in the 3D printed sample was distributed throughout the solid matrix and on pore/grain boundaries. The distribution and accessible surface area for each sample was calculated from X-ray CT images. Analysis of the images revealed that the amount of calcite on the surface was not even 0.5% of the total calcite present in the sample. In comparison with accessible calcite surface areas computed for a sandstone sample from the Paluxy formation in Qin and Beckingham (2019), the 3D printed samples had more than 50% smaller volume fraction of calcite and an order of magnitude lower accessible surface area. However, the surface area of calcite reported in Beckingham et al. (2017) was 2.14×10^{-5} $m^2/g \pm 1.14 \times 10^{-5}$ m^2/g for a sample with 0.03% calcite by volume. The lower accessible mineral surface area observed is attributed to the presence of clay coatings in the sample, which has been observed in other samples as well (Landrot et al. 2012; Waldmann et al. 2014). As such, 3D printing method can be viable for fabricating samples with replicate accessible mineral surface areas.

This work shows the feasibility of 3D printing samples containing reactive minerals and properties mimicking those of natural samples. Rock structure with pore network mimicking natural samples can be easily extracted from 3D X-ray CT images and serve as the basis for printed samples. Custom filaments containing mineral phases can be easily fabricated in the laboratory using common materials. These can be utilized in FDM printing where these printers are low-cost and widely available. However, it should be noted that currently the distribution of reactive mineral within the printed structure can't be controlled. In addition, there can be problems associated with printing samples with high amount of reactive mineral such as generation of unintended internal porosity due to incomplete overlap between layers or within

the same layer in the sample. Further studies in this field can help reduce problems observed in this study and improve our understanding of the parameters affecting mineral distribution in the 3D printed rock samples, thus facilitating better control over mineral distribution. This study made use of FDM technology for 3D printing. The possibility of achieving the same objective with other methods of 3D printing has yet to be explored and may offer some additional benefits and challenges to successful fabrication of synthetic reactive rocks.

2.6 Acknowledgement

Authors would like to acknowledge Dr. Eldon Triggs for allowing use of Lulbotz Taz4 3D printer and preliminary filament testing using their Filabot filament extruder. The author would also like to acknowledge undergraduate students Hayley Anderson and Shelby Wales for helping with the setup of acid resistance tests and filament fabrication. This work is supported by "Establishing an Early CO_2 Storage Complex in Kemper, Mississippi: Project ECO_2S" funded by the U.S. Department of Energy's National Energy Technology Laboratory and cost-sharing partners.

2.7 References

Al-Khulaifi, Yousef, Qingyang Lin, Martin J. Blunt, and Branko Bijeljic. 2018. "Reservoir-Condition Pore-Scale Imaging of Dolomite Reaction with Supercritical CO_2 acidified Brine: Effect of Pore-Structure on Reaction Rate Using Velocity Distribution Analysis." *International Journal of Greenhouse Gas Control* 68 (November 2017): 99–111. https://doi.org/10.1016/j.ijggc.2017.11.011.

Ameloot, Nele, Peter Maenhout, Stefaan De Neve, and Steven Sleutel. 2016. "Biochar-Induced N_2O Emission Reductions after Field Incorporation in a Loam Soil." *Geoderma* 267 (April): 10–16. https://doi.org/10.1016/J.GEODERMA.2015.12.016.

ASTM International. ASTM ISO/ASTM52900-15 Standard Terminology for Additive Manufacturing – General Principles – Terminology. West Conshohocken, PA; ASTM International, 2015. doi: https://doi.org/10.1520/ISOASTM52900-15

Bacher, Matthias, Andreas Schwen, and John Koestel. 2015. "Three-Dimensional Printing of Macropore Networks of an Undisturbed Soil Sample." *Vadose Zone Journal* 14 (2): 0. https://doi.org/10.2136/vzj2014.08.0111.

Bachu, Stefan, Didier Bonijoly, John Bradshaw, Robert Burruss, Sam Holloway, Niels Peter Christensen, and Odd Magne Mathiassen. 2007. "CO_2 Storage Capacity Estimation: Methodology and Gaps." *International Journal of Greenhouse Gas Control* 1 (4): 430–43. https://doi.org/10.1016/S1750-5836(07)00086-2.

Bachu, Stefan, W.D. Gunter, and E.H. Perkins. 1994. "Aquifer Disposal of CO_2: Hydrodynamic and Mineral Trapping." *Energy Conversion and Management* 35 (4): 269–79. https://doi.org/10.1016/0196-8904(94)90060-4.

Beckingham, L.E., C.A. Peters, W. Um, K.W. Jones, and W.B. Lindquist. 2013. "2D and 3D Imaging Resolution Trade-Offs in Quantifying Pore Throats for Prediction of Permeability." *Advances in Water Resources* 62 (December): 1–12. https://doi.org/10.1016/J.ADVWATRES.2013.08.010.

Beckingham, Lauren E., Elizabeth H. Mitnick, Carl I. Steefel, Shuo Zhang, Marco Voltolini, Alexander M. Swift, Li Yang, et al. 2016. "Evaluation of Mineral Reactive Surface Area Estimates for Prediction of Reactivity of a Multi-Mineral Sediment." *Geochimica et Cosmochimica Acta* 188 (September): 310–29. https://doi.org/10.1016/J.GCA.2016.05.040.

Beckingham, LE., Carl I. Steefel, Alexander M. Swift, Marco Voltolini, Li Yang, Lawrence M. Anovitz, Julia M. Sheets, et al. 2017. "Evaluation of Accessible Mineral Surface Areas for Improved Prediction of Mineral Reaction Rates in Porous Media." *Geochimica et Cosmochimica Acta* 205 (May): 31–49. https://doi.org/10.1016/J.GCA.2017.02.006.

Bhattacharjee, Nirveek, Arturo Urrios, Shawn Kang, and Albert Folch. 2016. "The Upcoming 3D-Printing Revolution in Microfluidics." *Lab on a Chip* 16 (10): 1720–42. https://doi.org/10.1039/c6lc00163g.

Black, Jay R., Susan A. Carroll, and Ralf R. Haese. 2015. "Rates of Mineral Dissolution under CO2storage Conditions." *Chemical Geology* 399: 134–44. https://doi.org/10.1016/j.chemgeo.2014.09.020.

Bourg, Ian C., Lauren E. Beckingham, and Donald J. DePaolo. 2015. "The Nanoscale Basis of CO_2 Trapping for Geologic Storage." *Environmental Science and Technology* 49 (17): 10265–84. https://doi.org/10.1021/acs.est.5b03003.

Bultreys, Tom, Wesley De Boever, and Veerle Cnudde. 2016. "Imaging and Image-Based Fluid

Transport Modeling at the Pore Scale in Geological Materials: A Practical Introduction to the Current State-of-the-Art." *Earth-Science Reviews* 155 (April): 93–128. https://doi.org/10.1016/J.EARSCIREV.2016.02.001.

Dal Ferro, N., and F. Morari. 2015. "From Real Soils to 3D-Printed Soils: Reproduction of Complex Pore Network at the Real Size in a Silty-Loam Soil." *Soil Science Society of America Journal* 79 (4): 1008. https://doi.org/10.2136/sssaj2015.03.0097.

Deng, Hang, Jeffrey P. Fitts, Dustin Crandall, Dustin McIntyre, and Catherine A. Peters. 2015. "Alterations of Fractures in Carbonate Rocks by CO_2-Acidified Brines." *Environmental Science and Technology* 49 (16): 10226–34. https://doi.org/10.1021/acs.est.5b01980.

Elhami, Ehsan, Maria Ask, and Hans Mattsson. 2016. "Physical- and Geomechanical Properties of a Drill Core Sample from 1.6 Km Depth at the Heletz Site in Israel: Some Implications for Reservoir Rock and CO_2 Storage." *International Journal of Greenhouse Gas Control* 48 (May): 84–93. https://doi.org/10.1016/J.IJGGC.2016.01.006.

Essaid, Hedeff I, Barbara A Bekins, and Isabelle M Cozzarelli. 2015. "Organic Contaminant Transport and Fate in the Subsurface: Evolution of Knowledge and Understanding." *Water Resources Research* 51 (7): 4861–4902. https://doi.org/10.1002/2015WR017121.

Goh, Kok-Hui, and Teik-Thye Lim. 2004. "Geochemistry of Inorganic Arsenic and Selenium in a Tropical Soil: Effect of Reaction Time, pH, and Competitive Anions on Arsenic and Selenium Adsorption." *Chemosphere* 55 (6): 849–59. https://doi.org/10.1016/J.CHEMOSPHERE.2003.11.041.

Guo, Nannan, and Ming C. Leu. 2013. "Additive Manufacturing: Technology, Applications and Research Needs." *Frontiers of Mechanical Engineering* 8 (3): 215–43.

https://doi.org/10.1007/s11465-013-0248-8.

Head, D., and T. Vanorio. 2016. “Effects of Changes in Rock Microstructures on Permeability: 3-D Printing Investigation.” *Geophysical Research Letters* 43 (14): 7494–7502. https://doi.org/10.1002/2016GL069334.

Hodder, Kevin J., John A. Nychka, and Rick J. Chalaturnyk. 2018. “Process Limitations of 3D Printing Model Rock.” *Progress in Additive Manufacturing* 3 (3): 173–82. https://doi.org/10.1007/s40964-018-0042-6.

Hunter, Kimberley S., Yifeng Wang, and Philippe Van Cappellen. 1998. “Kinetic Modeling of Microbially-Driven Redox Chemistry of Subsurface Environments: Coupling Transport, Microbial Metabolism and Geochemistry.” *Journal of Hydrology* 209 (1–4): 53–80. https://doi.org/10.1016/S0022-1694(98)00157-7.

Ishutov, Sergey, Franciszek J. Hasiuk, Chris Harding, and Joseph N. Gray. 2015. “3D Printing Sandstone Porosity Models.” *Interpretation* 3 (3): SX49–61. https://doi.org/10.1190/INT-2014-0266.1.

Ishutov, Sergey, Franciszek J. Hasiuk, Dawn Jobe, and Susan Agar. 2018. “Using Resin-Based 3D Printing to Build Geometrically Accurate Proxies of Porous Sedimentary Rocks.” *Groundwater* 56 (3): 482–90. https://doi.org/10.1111/gwat.12601.

Jiang, Chao, and Gao-Feng Zhao. 2015. “A Preliminary Study of 3D Printing on Rock Mechanics.” *Rock Mechanics and Rock Engineering* 48 (3): 1041–50. https://doi.org/10.1007/s00603-014-0612-y.

Jiang, Quan, Xiating Feng, Lvbo Song, Yahua Gong, Hong Zheng, and Jie Cui. 2016. “Modeling

Rock Specimens through 3D Printing: Tentative Experiments and Prospects." *Acta Mechanica Sinica* 32 (1): 101–11. https://doi.org/10.1007/s10409-015-0524-4.

Jin, Qusheng, and Craig M. Bethke. 2005. "Predicting the Rate of Microbial Respiration in Geochemical Environments." *Geochimica et Cosmochimica Acta* 69 (5): 1133–43. https://doi.org/10.1016/J.GCA.2004.08.010.

Josh, M., L. Esteban, C. Delle Piane, J. Sarout, D.N. Dewhurst, and M.B. Clennell. 2012. "Laboratory Characterisation of Shale Properties." *Journal of Petroleum Science and Engineering* 88–89 (June): 107–24. https://doi.org/10.1016/J.PETROL.2012.01.023.

Jung, Heewon, and Alexis Navarre-Sitchler. 2018. "Scale Effect on the Time Dependence of Mineral Dissolution Rates in Physically Heterogeneous Porous Media." *Geochimica et Cosmochimica Acta* 234 (August): 70–83. https://doi.org/10.1016/J.GCA.2018.05.009.

Kong, Lingyun, Mehdi Ostadhassan, Xiaodong Hou, Michael Mann, and Chunxiao Li. 2019. "Microstructure Characteristics and Fractal Analysis of 3D-Printed Sandstone Using Micro-CT and SEM-EDS." *Journal of Petroleum Science and Engineering* 175 (April): 1039–48. https://doi.org/10.1016/J.PETROL.2019.01.050.

Lambkin, Denise C., Kerry H. Gwilliam, Caroline Layton, Matt G. Canti, Trevor G. Piearce, and Mark E. Hodson. 2011. "Production and Dissolution Rates of Earthworm-Secreted Calcium Carbonate." *Pedobiologia* 54 (December): S119–29. https://doi.org/10.1016/J.PEDOBI.2011.09.003.

Landrot, Gautier, Jonathan B. Ajo-Franklin, Li Yang, Stefano Cabrini, and Carl I. Steefel. 2012. "Measurement of Accessible Reactive Surface Area in a Sandstone, with Application to CO_2 Mineralization." *Chemical Geology* 318–319: 113–25.

https://doi.org/10.1016/j.chemgeo.2012.05.010.

Ligon, Samuel Clark, Robert Liska, Jürgen Stampfl, Matthias Gurr, and Rolf Mülhaupt. 2017. "Polymers for 3D Printing and Customized Additive Manufacturing." *Chemical Reviews* 117 (15): 10212–90. https://doi.org/10.1021/acs.chemrev.7b00074.

Liu, Kouqi, Mehdi Ostadhassan, Jie Zhou, Thomas Gentzis, and Reza Rezaee. 2017. "Nanoscale Pore Structure Characterization of the Bakken Shale in the USA." *Fuel* 209 (August): 567–78. https://doi.org/10.1016/j.fuel.2017.08.034.

Loeb, Stephanie K, Jun Kim, Chenxi Jiang, Lawrence Stephen Early, Haoran Wei, Qilin Li, and Jae-Hong Kim. 2019. "Nanoparticle Enhanced Interfacial Solar Photothermal Water Disinfection Demonstrated in 3-D Printed Flow-Through Reactors." *Environmental Science & Technology*, June, acs.est.9b01142. https://doi.org/10.1021/acs.est.9b01142.

Mcdonald, J Cooper, and George M Whitesides. 2002. "Poly(Dimethylsiloxane) as a Material for Fabricating Microfluidic Devices." *ACCOUNTS OF CHEMICAL RESEARCH* 35 (7): 491–99. https://doi.org/10.1021/ar010110q.

Molins, Sergi, David Trebotich, Carl I. Steefel, and Chaopeng Shen. 2012. "An Investigation of the Effect of Pore Scale Flow on Average Geochemical Reaction Rates Using Direct Numerical Simulation." *Water Resources Research* 48 (3): 1–11. https://doi.org/10.1029/2011WR011404.

Molins, Sergi, David Trebotich, Li Yang, Jonathan B. Ajo-Franklin, Terry J. Ligocki, Chaopeng Shen, and Carl I. Steefel. 2014. "Pore-Scale Controls on Calcite Dissolution Rates from Flow-through Laboratory and Numerical Experiments." *Environmental Science and Technology* 48 (13): 7453–60. https://doi.org/10.1021/es5013438.

Otten, W., R. Pajor, S. Schmidt, P.C. Baveye, R. Hague, and R.E. Falconer. 2012. “Combining X-Ray CT and 3D Printing Technology to Produce Microcosms with Replicable, Complex Pore Geometries.” *Soil Biology and Biochemistry* 51 (August): 53–55. https://doi.org/10.1016/J.SOILBIO.2012.04.008.

Peng, Cheng, John P. Crawshaw, Geoffrey C. Maitland, and J. P.Martin Trusler. 2015. “Kinetics of Calcite Dissolution in CO_2-Saturated Water at Temperatures between (323 and 373)K and Pressures up to 13.8MPa.” *Chemical Geology* 403: 74–85. https://doi.org/10.1016/j.chemgeo.2015.03.012.

Pereira Nunes, J. P., B. Bijeljic, and M. J. Blunt. 2016. “Pore-Space Structure and Average Dissolution Rates: A Simulation Study.” *Water Resources Research* 52 (9): 7198–7212. https://doi.org/10.1002/2016WR019313.

Plummer, L Niel, and T. M. L. WIGLEY. 1976. “The Dissolution of Calcite in CO_2-Saturated Solutions at 25°C and 1 Atmosphere Total Pressure.” *Geochlmlca et Cosmochlmlca Acta* 40: 191–202.

Qin, Fanqi, and Lauren E. Beckingham. 2019. “Impact of Image Resolution on Quantification of Mineral Abundances and Accessible Surface Areas.” *Chemical Geology* 523 (September): 31–41. https://doi.org/10.1016/j.chemgeo.2019.06.004.

Rathnaweera, T. D., P. G. Ranjith, and M. S. A. Perera. 2016. “Experimental Investigation of Geochemical and Mineralogical Effects of CO_2 Sequestration on Flow Characteristics of Reservoir Rock in Deep Saline Aquifers.” *Scientific Reports* 6 (1): 19362. https://doi.org/10.1038/srep19362.

Ross, Graham D., Adrain C. Todd, John A. Tweedie, and Andrew G.S. Will. 1982. “The

Dissolution Effects of CO_2-Brine Systems on the Permeability of U.K. and North Sea Calcareous Sandstones." In *SPE Enhanced Oil Recovery Symposium*. Society of Petroleum Engineers. https://doi.org/10.2118/10685-MS.

Rusling, James F. 2018. "Developing Microfluidic Sensing Devices Using 3D Printing." https://doi.org/10.1021/acssensors.8b00079.

Sandhu, Daljit, Arvind Singh, Steven J. Duranceau, Boo Hyun Nam, Talea Mayo, and Dingbao Wang. 2018. "Fate and Transport of Radioactive Gypsum Stack Water Entering the Floridan Aquifer Due to a Sinkhole Collapse." *Scientific Reports* 8 (1): 11439. https://doi.org/10.1038/s41598-018-29541-0.

Shiraki, Ryoji, and Thomas L. Dunn. 2000. "Experimental Study on Water–Rock Interactions during CO_2 Flooding in the Tensleep Formation, Wyoming, USA." *Applied Geochemistry* 15 (3): 265–79. https://doi.org/10.1016/S0883-2927(99)00048-7.

Silva, G. P.D. De, P. G. Ranjith, and M. S.A. Perera. 2015. "Geochemical Aspects of CO_2 Sequestration in Deep Saline Aquifers: A Review." *Fuel* 155: 128–43. https://doi.org/10.1016/j.fuel.2015.03.045.

Vishal, V., P.G. Ranjith, and T.N. Singh. 2015. "An Experimental Investigation on Behaviour of Coal under Fluid Saturation, Using Acoustic Emission." *Journal of Natural Gas Science and Engineering* 22 (January): 428–36. https://doi.org/10.1016/J.JNGSE.2014.12.020.

Waldmann, Svenja, Andreas Busch, Kees van Ojik, and Reinhard Gaupp. 2014. "Importance of Mineral Surface Areas in Rotliegend Sandstones for Modeling CO_2–Water–Rock Interactions." *Chemical Geology* 378–379 (June): 89–109. https://doi.org/10.1016/J.CHEMGEO.2014.03.014.

Wen, Hang, and Li Li. 2018. “An Upscaled Rate Law for Mineral Dissolution in Heterogeneous Media: The Role of Time and Length Scales.” *Geochimica et Cosmochimica Acta* 235 (August): 1–20. https://doi.org/10.1016/J.GCA.2018.04.024.

Xiong, Wei, Rachel K. Wells, Jake A. Horner, Herbert T. Schaef, Philip A. Skemer, and Daniel E. Giammar. 2018. “CO_2 Mineral Sequestration in Naturally Porous Basalt.” *Environmental Science and Technology Letters* 5 (3): 142–47. https://doi.org/10.1021/acs.estlett.8b00047.

Yu, Zhichao, Li Liu, Siyu Yang, Shi Li, and Yongzhi Yang. 2012. “An Experimental Study of CO_2–Brine–Rock Interaction at in Situ Pressure–Temperature Reservoir Conditions.” *Chemical Geology* 326–327 (October): 88–101. https://doi.org/10.1016/J.CHEMGEO.2012.07.030.

Zhu, Daoyi, Jirui Hou, Jianfei Wang, Xuan Wu, Peng Wang, and Baojun Bai. 2018. “Acid-Alternating-Base (AAB) Technology for Blockage Removal and Enhanced Oil Recovery in Sandstone Reservoirs.” *Fuel* 215 (March): 619–30. https://doi.org/10.1016/J.FUEL.2017.11.090.

Zou, Yushi, Sihai Li, Xinfang Ma, Shicheng Zhang, Ning Li, and Ming Chen. 2018. “Effects of CO_2–Brine–Rock Interaction on Porosity/Permeability and Mechanical Properties during Supercritical-CO_2 fracturing in Shale Reservoirs.” *Journal of Natural Gas Science and Engineering* 49 (November 2017): 157–68. https://doi.org/10.1016/j.jngse.2017.11.004.

Chapter 3: 3D flow and transport simulation at pore scale using OpenFOAM

3.1 Abstract

CO_2 storage in deep saline aquifers is a promising means of reducing atmospheric CO_2 emissions. Once injected, CO_2 dissolves in formation brine and reacts with minerals resulting in dissolution reactions that potentially alter formation properties including porosity and permeability. The rate and extent of these reactions and corresponding impact on permeability, however, is not well understood. Accurate understanding of these reactions at pore scale, where physical interaction occurs, is important to assess long-term effects of these reactions on the rock formation. Direct numerical simulation has emerged as a powerful means of pore scale simulation. In this work, the change in distribution of ions in the Paluxy formation due to CO_2 injection is simulated using OpenFOAM, an open source computational fluid dynamics (CFD) software. While this software has been used extensively for flow in porous media, it has seldom been used for simulating reactive flow as it doesn't have capabilities to simulate geochemical reactions in a 3D mesh of real porous media by itself. In this work, a 3D pore network mesh is generated from 3D X-ray Computed Tomography images of a sandstone sample from the Paluxy formation. Fluid flow is simulated in the pore space by solving the Navier-Stokes equation coupled with continuity conservation and the transport of ions was simulated using the advection-diffusion equation. The flow and transport simulations here will be used to develop a solver simulating dissolution and precipitation reactions, incorporating a dynamic mesh

and integrated kinetic mineral reactions in multi-mineralic porous media.

3.2 Introduction

Permanent storage of CO_2 in subsurface geological formations has been suggested as a way for reducing anthropogenic CO_2 emissions (Holloway 2005). Potential geological CO_2 storage systems include depleted oil and gas reservoirs (Bachu et al. 1994), unminable coal seams (Gale 2004) and deep saline aquifers (De Silva et al. 2015). Of these, deep saline aquifers have the highest potential for storing CO_2 (1627-20,176 Gt) followed by unmineable coal seams (61-119 Gt) and depleted oil and gas reservoirs (84 Gt) (Wright et al. 2013). CO_2 injection into deep saline aquifers results in changes in the geochemical equilibrium of the system including lowering of pH (Steefel et al. 2013) and subsequent reaction with formation minerals (Molins et al. 2014) and changes in porosity and permeability (Rathnaweera et al. 2016). Estimation of these changes can be either done by experimentation or using numerical simulation.

Experiments on CO_2 reservoir rocks studying changes in porosity, permeability, pH and reactions, span from days to a few years (Kaszuba et al. 2003; Rosenbauer et al. 2005; Kaszuba et al. 2005; Soong et al. 2014; Rathnaweera et al. 2016; Beckingham et al. 2013; Deng et al. 2015). Mineral trapping of CO_2, which is the most stable form of storage, is a slow and long-term process which is anticipated to take hundreds to thousands of years to complete (De Silva et al. 2015). Experimental studies are at a disadvantage at predicting this process completely, due to the limitation of time scale at which these experiments can be run. Furthermore, experimental analysis of host rocks is time-consuming, expensive and sometimes not feasible in the laboratory (Zhang et al. 2015). Running experiments, such as flow through experiment or batch reactor experiment, with different parameters on the same host rock would be meaningless as the sample

properties change after its use for the first time. Numerical modelling is a viable option to overcome these disadvantages where simulations can be run for much longer time periods and multiple simulations can be carried out on the same sample (Xu et al. 2011; Gherardi et al. 2012; Soulaine et al. 2017; Horgue et al. 2015; Liu et al. 2018).

Numerical modelling depends on the scale of the system (Jung and Navarre-Sitchler 2018; Li et al. 2008; Steefel et al. 2005) i.e. whether the simulation is done at continuum scale, where representative element volume is considered (Molins et al. 2012; Gherardi et al. 2012; Beckingham et al. 2017; Iraola et al. 2019) or at the pore scale, where parameters can be subsequently upscaled to the continuum scale (Noiriel et al. 2012; Kang et al. 2010; Li et al. 2006; Deng et al. 2018; Apourvari and Arns 2016). There are some approximations involved in the case of continuum scale simulations such as estimating the surface area of reactive minerals, intrinsic reaction rates and rate constants etc. (Peters 2009; Li et al. 2006; Mostaghimi et al. 2016; Beckingham et al. 2017). Pore scale simulations have the advantage of directly accounting for these approximations (Noiriel et al. 2012).

Pore scale simulations can be divided into two types: direct numerical simulations (DNS) and pore network models (PNM). DNS involves solving governing equations for flow and transport on a domain representing natural rock samples (Liu and Mostaghimi 2018; Molins 2015; Siena et al. 2015; Watson et al. 2018), whereas PNM involves simplification of pore space into connections of pores and pore throats (Steinwinder and Beckingham 2019; Li, Peters, and Celia 2006; Beckingham et al. 2013; Nogues et al. 2013; Shah et al. 2016). PNM is computationally more efficient due to the simplification of the pore network (Varloteaux et al. 2013) as compared to DNS as DNS simulates Navier-Stokes equation in actual complex pore geometries mostly for low Reynolds number flow. DNS has been used in various ways for

simulating fluid flow, transport of ions and geochemical reactions. Molins et al. (2012) simulated flow and reactive transport using Chombo and Crunchflow. Mostaghimi et al. (2013) used DNS to simulate flow and estimate permeability in a 3D geometry generated from X-ray CT images of rock. Siena et al. (2015) compared flow field simulated with three fluid dynamics software using different numerical methods and algorithms. Zhu et al. (2016) simulated fluid displacement due to injection of immiscible fluid into the pore scale porous media. Soulaine et al. (2018) proposed a method to simulate multi-fluid reactive transport system at pore scale. Starchenko et al. (2016) developed an extension of OpenFOAM source code involving mesh motion as well as relaxation to incorporate changes in pore space resulting from dissolution in the fractures. Though DNS has been used for different systems using myriad of software and numerical schemes, the DNS is used here to understand the pore scale distribution of Ca^{2+}, H^{+} and HCO_3^{-} ions during CO_2 injection in saline aquifer in context of Paluxy formation.

Here, a pore scale mesh was generated from X-ray CT images of a sandstone sample. Fluid flow and the transport of ions through the mesh were then simulated using OpenFOAM. OpenFOAM is an open-source C++ based software that solves partial differential equations using the finite volume method (www.openfoam.org). OpenFOAM has been used for simulating three-dimensional flow and has shown excellent parallel processing capabilities, but it has not been used frequently for simulating reactive transport on a mesh representing a real rock sample (Mostaghimi et al. 2013; Orgogozo et al. 2014; Guibert et al. 2015; Horgue et al. 2015; Aboukhedr et al. 2015; Oliveira et al. 2019; Al-Khulaifi et al. 2017, 2018). This work will serve as the basis for development of a reactive direct numerical simulation model of multi-mineralic porous media with integrated dynamic mesh to account for pore structure changes resulting from mineral dissolution and precipitation reactions.

3.3 Methods

3.3.1 Sample description and mesh generation

The sample considered in this study is a sandstone sample from Paluxy formation in Kemper county, Mississippi. It is the same sample considered in Chapter 2 of this thesis. In the previous chapter, mesh was generated corresponding to the grains in the sample, whereas here a wavefront (.obj) mesh was generated corresponding to the pores in the subsample. The mesh was also processed in Blender to remove unconnected regions and the final mesh was exported as a stereolithography (.stl) file as shown in Figure 3.1 (b).

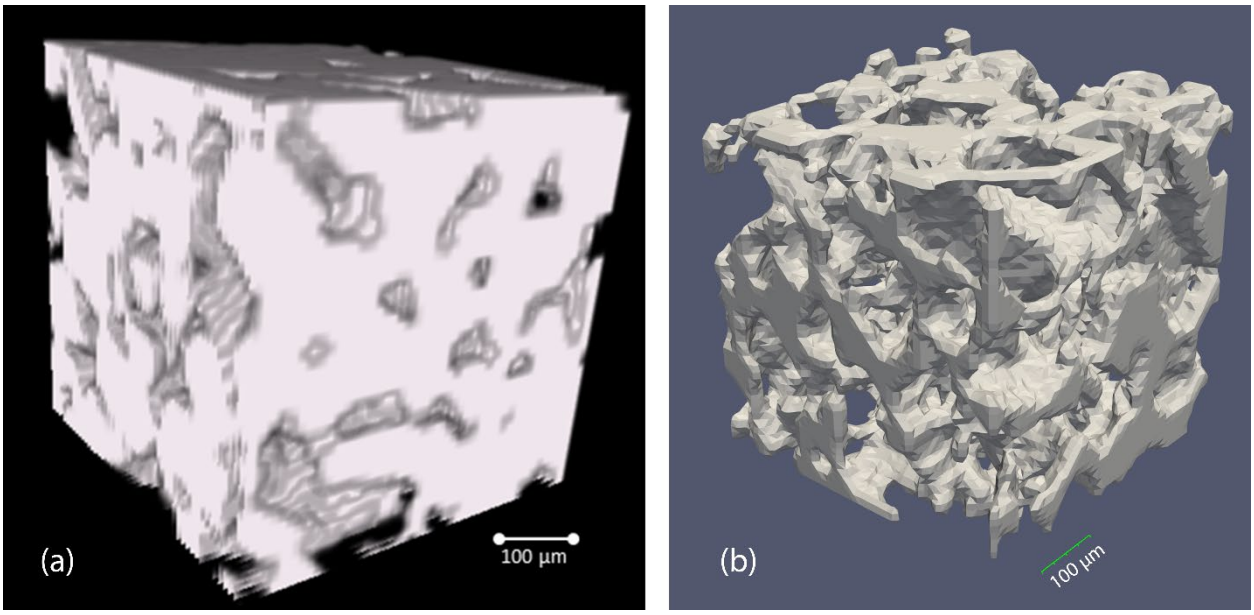

Figure 3.1: (a) X-ray CT image of the subsample selected from sandstone sample from Paluxy formation (b) Mesh corresponding to pore space in subsample.

3.3.2 Simulated system

The system considered in this study is an actual pore network of rock sample from a saline aquifer which will undergo CO_2 injection. When CO_2 in gaseous phase is injected into deep

saline formations, it becomes supercritical fluid under high temperature and pressure of the formation. This supercritical fluid dissolves into brine forming carbonic acid. Carbonic acid dissociates giving rise to H^+ ions and reduce the pH of the system. Equation 3.1 - 3.3, shows reactions that will happen due to injection of CO_2 into saline formations.

$$CO_{2(g)} \leftrightarrow CO_{2(sc)} \tag{3.1}$$

$$CO_{2(sc)} + H_2O \leftrightarrow H_2CO_3 \tag{3.2}$$

$$H_2CO_3 \leftrightarrow HCO_3^- + H^+ \tag{3.3}$$

Under the low pH conditions generated due to injection of CO_2, reactive minerals in the saline aquifer formation may undergo dissolution reactions. For simplicity, calcite is assumed to be the only reactive phase in the formation for this work. Calcite dissolution can occur in three parallel pathways (Equations 3.4 - 3.6) (Plummer et al. 1978), where only the second pathway was considered here.

$$CaCO_{3(s)} + H^+ \leftrightarrow Ca^{++} + HCO_3^- \tag{3.4}$$

$$CaCO_{3(s)} + H_2CO_3 \leftrightarrow Ca^{++} + 2HCO_3^- \tag{3.5}$$

$$CaCO_{3(s)} + H_2O \leftrightarrow Ca^{++} + HCO_3^- + OH^- \tag{3.6}$$

Initially, the system is filled with brine containing 7 x 10^{-4} mol/kg $Ca^{+2,}$ 7.94 x 10^{-8} mol/kg of H^+ and very low (1 x 10^{-30} mol/kg) concentration of HCO_3^-. These values depict the natural equilibrium conditions in saline aquifers. To reflect CO_2 injection, a constant inflow of H^+ and HCO_3^- ions into the system is considered. Fluid flow into the system was simulated using the Navier-Stokes (Equation 3.7) and continuity equation (Equation 3.8) and the transport of ions was simulated using the advection-diffusion equation (Equation 3.9).

$$\partial_t u + \nabla \cdot (uu) + \nabla p = \nu \nabla^2 u + f \tag{3.7}$$

$$\nabla \cdot u = 0 \tag{3.8}$$

$$\partial_t c + \nabla \cdot (uc) = D\nabla^2 c \tag{3.9}$$

where, u is the fluid velocity vector, p is the pressure, v is kinematic viscosity, f is body forces and C is the concentration of the ion being transported. Of all these parameters, only fluid velocity is vector and all other parameters are scalar quantities.

3.3.3 Simulation description

The simulation domain is shown in Figure 3.2. The red face shows the inlet boundary, while the green face is the outlet boundary and the white faces are the sides. The mesh, shown in blue, is the pore space through which flow of fluid and transport of ions is simulated.

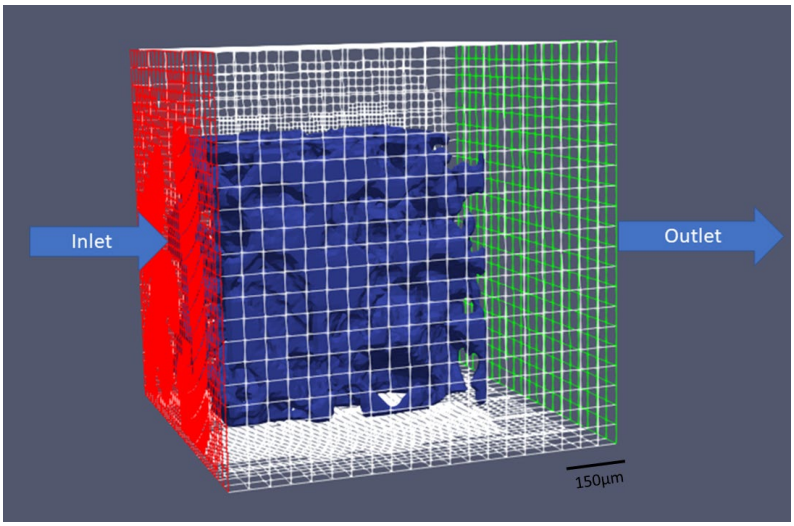

Figure 3.2: Simulated domain showing inlet (red face), outlet (green face), sides (white faces) and the pore space mesh (blue region).

The simulation is made up of two components: a flow solver and a transport solver. For the flow simulation, the incompressible, laminar and steady state flow solver, simpleFoam, was used. SimpleFoam uses the continuity equation and Navier-Stokes equation to calculate the flow

field. The boundary conditions for flow solver include velocity of 4 x 10^{-5} m/s, or 3.5 m/day at the inlet (Gelhar et al. 1955) and zero velocity gradient at the outlet. The pressure at outlet was fixed at 0 m^2/s^2, whereas the pressure at the inlet was kept as zero gradient. No slip boundary conditions for velocity and a zero gradient for pressure is set for the four sides. The walls of the mesh is set at zero gradient for all the simulations. Initially, the velocity and pressure were set to 0 for all the internal parts of the mesh. The kinematic viscosity of the fluid was 0.001m^2/s. Flow was simulated until the steady state condition is reached.

The steady state flow field is then used as input to the transport solver, scalarTransportFoam, which uses the advection-diffusion equation for transport of ions in our system. With the transport solver, the transport of three ions (Ca^{+2}, H^+ and HCO_3^-) are simulated using the advection-diffusion equation. The diffusion coefficients of Ca^{+2}, H^+ and HCO_3^- at 25°C were obtained from PHREEQC database as shown in Table 3.1. The initial and boundary condition of ions were set as shown in Table 3.2. At the inlet, constant input of ions depicting injection of supercritical CO_2 was specified and a zero gradient of concentration of ions was specified for the outlet boundary condition for all ions. A no slip boundary condition was specified for the sides. This unsteady state transport solver was run with timestep of 0.001 seconds until steady state was reached. Time step for transport solver was selected in order to keep the courant number below 1, which results in stable numerical model.

Table 3.1: Diffusion constant of ions at 25°C.

Ion	Diffusion Constant (m^2/s)
Ca^{+2}	0.79 x 10^{-9}
H^+	2.35 x 10^{-9}
HCO_3^-	1.18 x 10^{-9}

Table 3.2: Initial condition of ions in transport solver

Ion	Initial Concentration (mol/kg)	Boundary condition at inlet (mol/kg)
Ca^{+2}	7×10^{-4}	1×10^{-30}
H^{+}	7.94×10^{-8}	3.16×10^{-4}
HCO_3^{-}	1×10^{-30}	7.68×10^{-4}

The results of the simulation are visualized in Paraview v5.6.0-RC1. The magnitude of the velocity calculated for each cell of the mesh at steady state is determined and histograms of velocity and pressure fields are generated.

3.4 Results and Discussion

The flow solver reached steady state after 543 iterations. The result from the flow simulation are shown in Figure 3.3, 3.4 and 3.5. Figure 3.3 shows the velocity for different regions of the mesh as well the histogram of velocities. Here, regions with velocities greater than 1 mm/s are shown in red while slower velocities are shown in blue. The maximum velocity observed was 6.7 mm/s in the regions closer to the outlet with Reynolds number close to 10^{-3}. The majority of the regions in the mesh had velocities less than 1 mm/s. Higher velocity in certain regions may be attributed to the smaller pore throats. Figure 3.4 shows the velocity field after 300, 400, 500 and 543 iterations of flow solver. It can be observed that there is generation of preferential flow path along the middle of the mesh as evident by the presence of higher velocity zone.

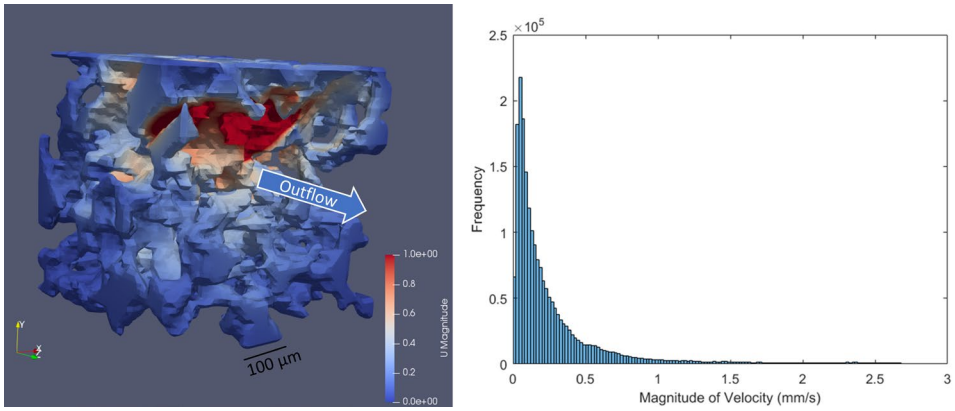

Figure 3.3: Velocity (in mm/s) in different regions of the pore space mesh on the left and histogram of magnitude of velocities on the right at steady state.

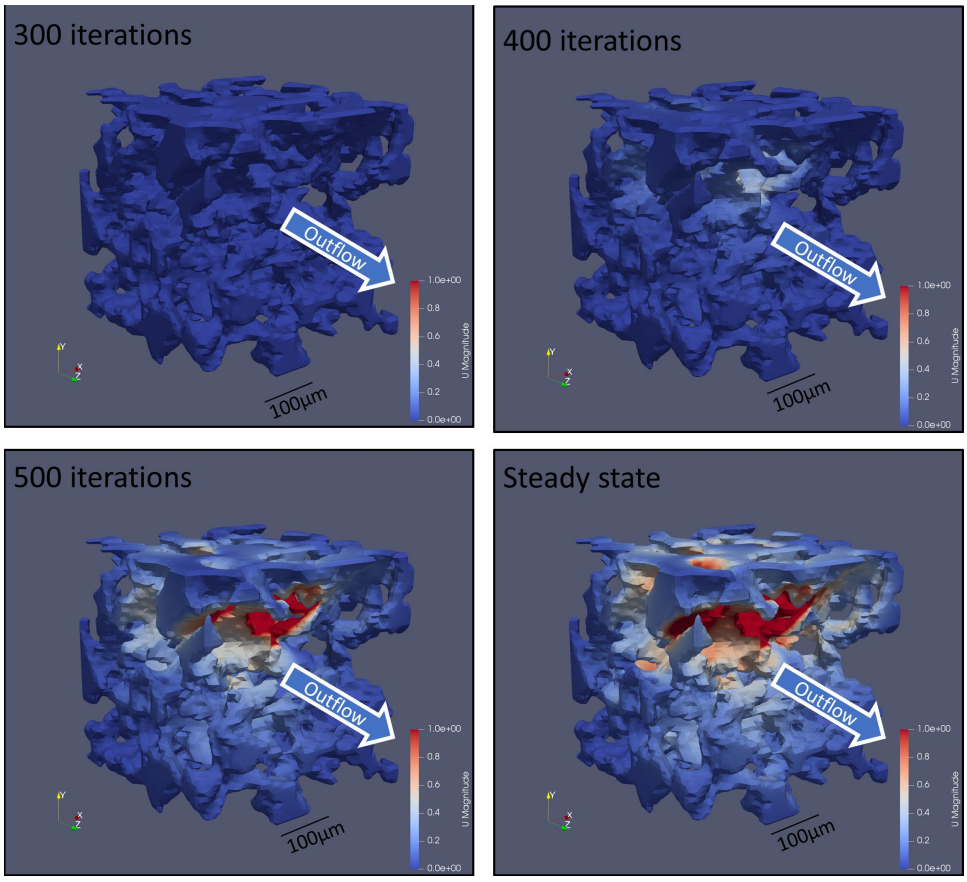

Figure 3.4: Velocity (in mm/s) in different regions of the pore space mesh after (a) 300, (b) 400, (c) 500 and (d) 543 (steady state) iteration of flow solver.

Figure 3.5 shows the kinematic pressure distribution and histogram of kinematic pressure values. The unit of pressure used here is m^2/s^2 and is relative to the outlet pressure of 0 m^2/s^2. It is found that the majority of the regions have negative pressure values, meaning they have lower pressure as compared to outlet but the pressure is lowest along the preferential flow path. Also, it is observed that the regions with higher velocity had low pressure and vice versa which is accordance with the Darcy's law, as velocity is inversely proportional to difference in pressure. These results hold true for natural system as the regions with low pressure tend to have higher velocity in pressure driven systems.

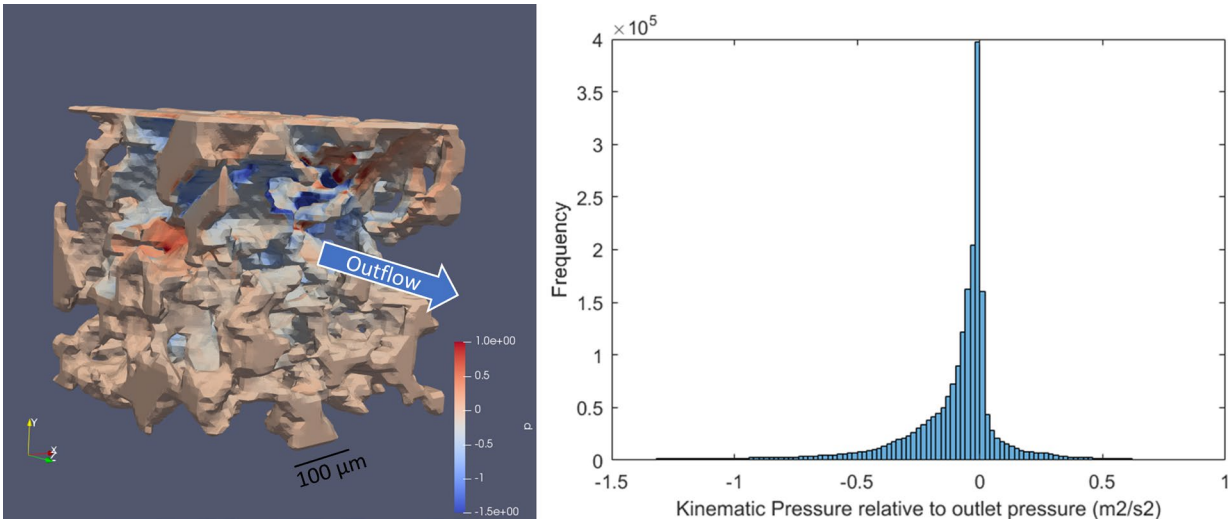

Figure 3.5: Kinematic pressure in different regions of the pore space mesh relative to outlet pressure on the left and histogram of kinematic pressure values on the right at steady state.

The result from the unsteady state transport solver are shown in Figure 3.6, 3.7 and 3.8. The concentration of the three simulated ions is shown at some initial time steps as well as when it reached steady state. The steady state concentration of Ca^{+2}, H^+ and HCO_3^- reached in 3.9 sec, 4.0 sec and 6.0 sec respectively. The longer time required to reach steady state for HCO_3^- is

attributed to the higher difference between the initial and inlet boundary condition. The differences in the concentration at different regions of the mesh is due to the heterogeneity in the pore structure. Some areas have higher concentration, represented by red color in the figures, while other regions have lower concentration values, shown in dark blue color. When the steady state of the three ions are compared it is observed that it is almost similar to each other. There are differences in concentration in areas with lower velocity. This is due to the advection being dominant in regions with higher velocity, while the differences in concentration in lower velocity regions is due to the diffusion.

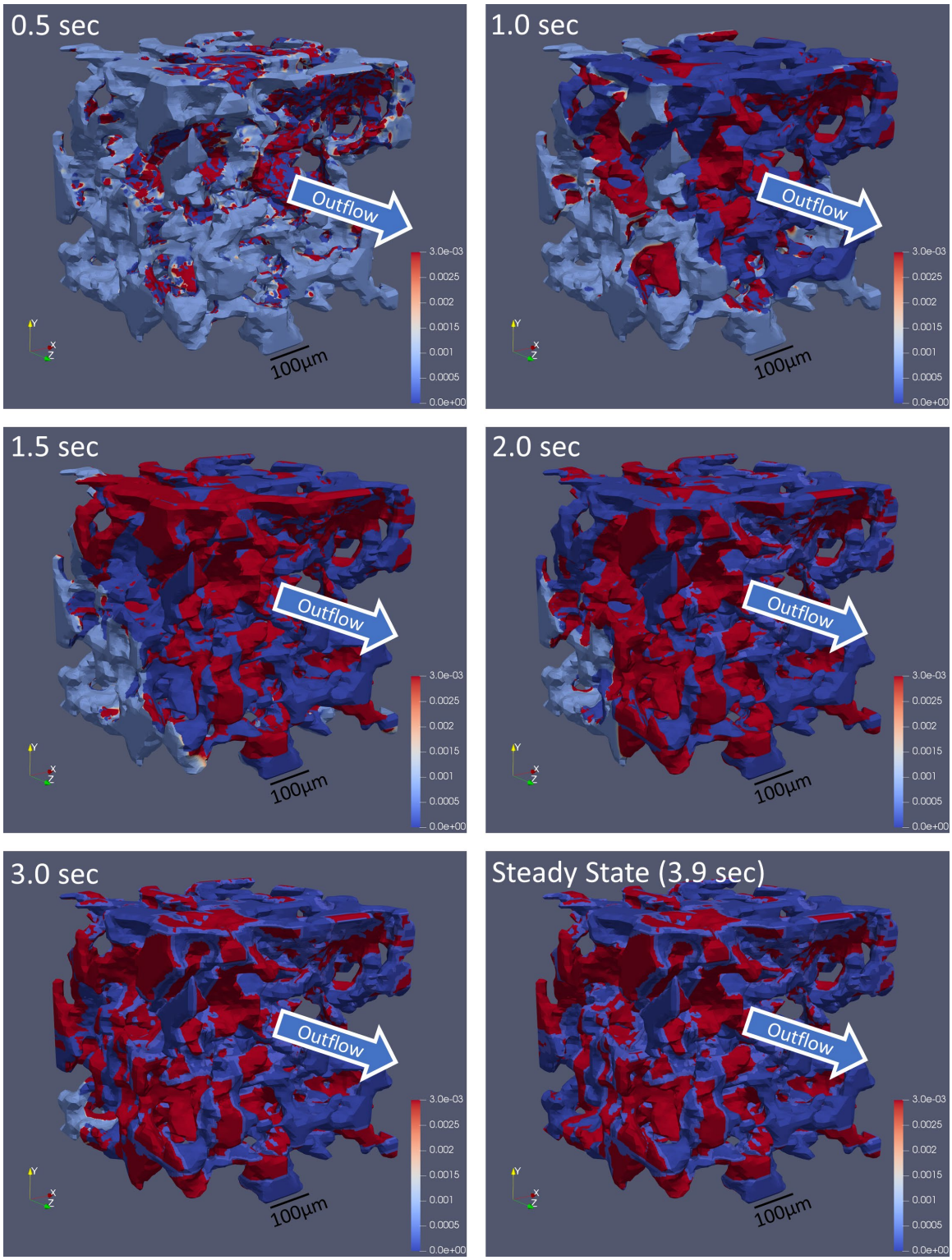

Figure 3.6: Concentration of Ca^{+2} at different times and at steady state. (a) 0.5 sec, (b) 1.0 sec, (c) 1.5 sec, (d) 2.0 sec, (e) 3.0 sec, (f) Steady state

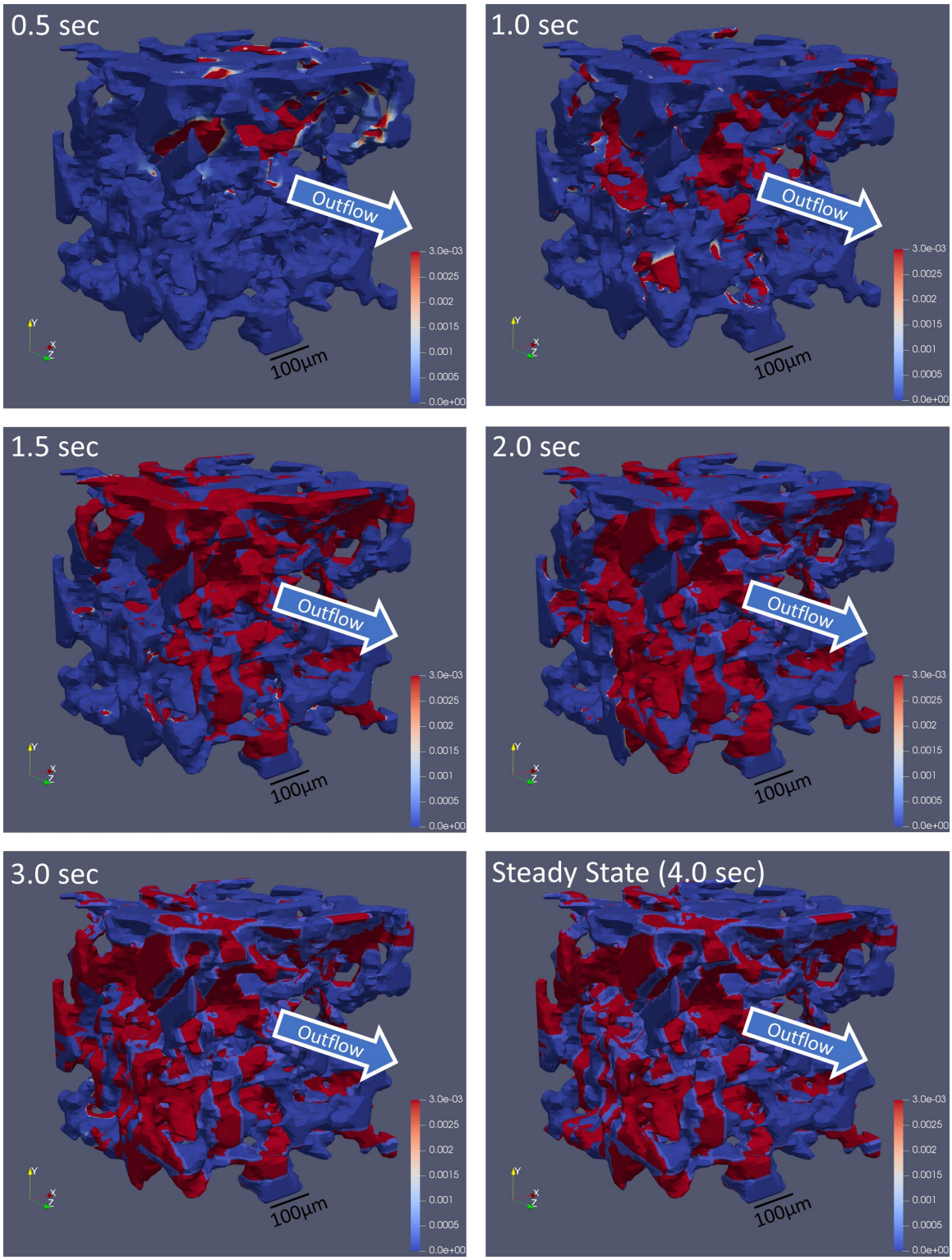

Figure 3.7: Concentration of H^+ at different times and at steady state. (a) 0.5 sec, (b) 1.0 sec, (c) 1.5 sec, (d) 2.0 sec, (e) 3.0 sec, (f) steady state

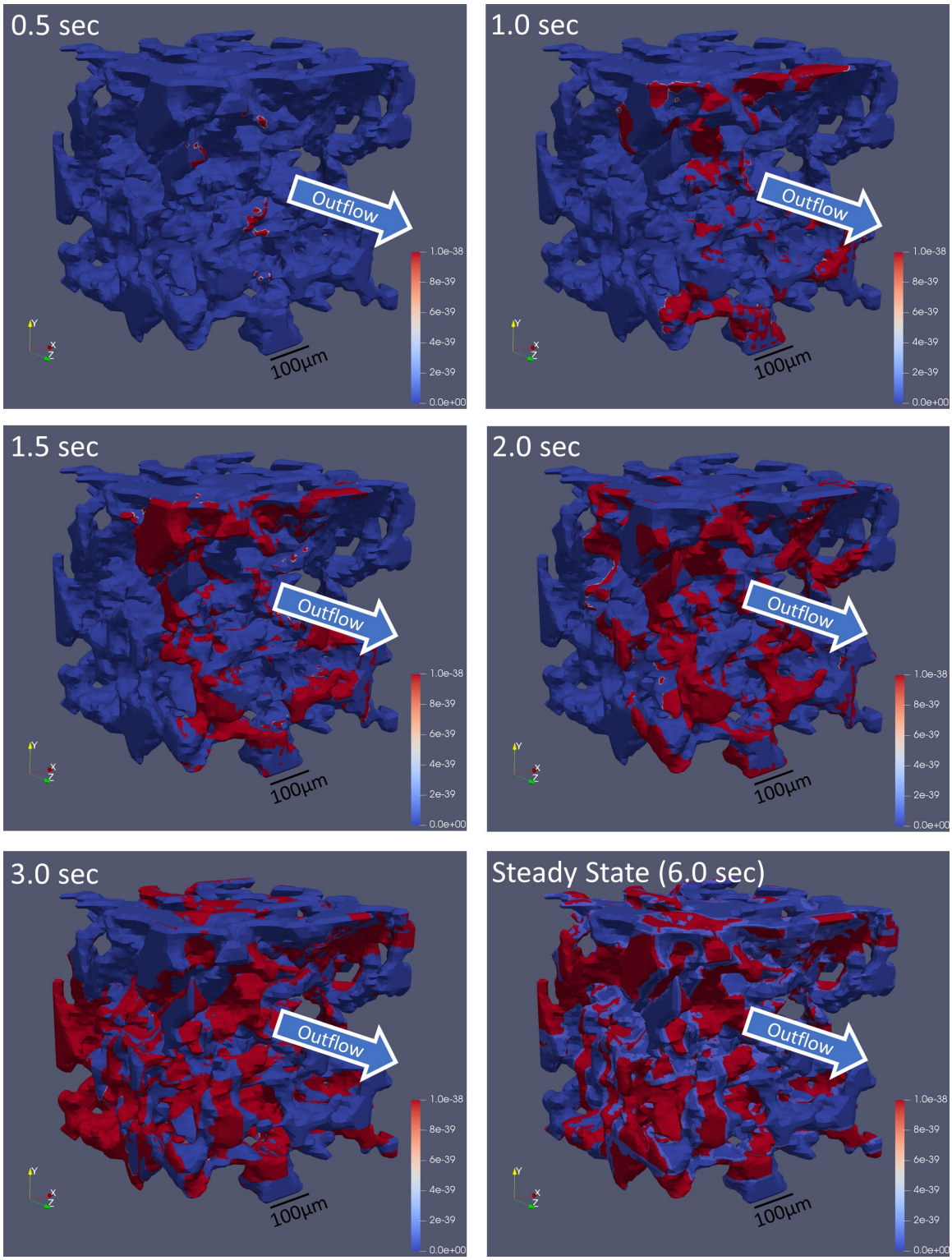

Figure 3.8: Concentration of HCO_3^- at different times and at steady state. (a) 0.5 sec, (b) 1.0 sec, (c) 1.5 sec, (d) 2.0 sec, (e) 3.0 sec, (f) steady state

3.5 Conclusion

OpenFOAM, an open source CFD software was used here to simulated fluid flow and transport of ions through pore space mesh generated from the X-ray CT images of a sample extracted from the Paluxy formation in Kemper County, Mississippi. Flow was simulated using Navier-Stokes and continuity equation and transport of ions was simulated using advection-diffusion equation. The simulation was run until steady state conditions were achieved.

The steady state flow field saw development of preferential flow path along the middle of the mesh, with a maximum velocity of 6.7 mm/s. The velocity and pressure fields were inversely correlated to each other. There were differences in concentration of ions in different regions of the mesh due to the heterogeneous pore space. Also, the effect of advection and diffusion were observed in different regions of the mesh. In conclusion, OpenFOAM was used to understand the distribution of ions during CO_2 injection in Paluxy formation.

The flow and transport simulation studied here will be used to develop a new OpenFOAM solver with the capability of simulating mineral dissolution/precipitation reactions in geologic porous samples. The new solver will be able to calculate the rate of reaction based on transition state theory rate law as well as update pore space mesh depending on the amount of minerals dissolved or precipitated. Updating of pore space mesh would involve mesh motion and relaxation. With the development of this solver, direct numerical simulation of geochemical reactions in multi-mineralic porous media can be implemented.

3.6 Acknowledgement

This work is supported by "Establishing an Early CO_2 Storage Complex in Kemper, Mississippi: Project ECO_2S" funded by the U.S. Department of Energy's National Energy Technology Laboratory and cost-sharing partners.

3.7 References

Bacon, Diana H., Bruce M. Sass, Mohit Bhargava, Joel Sminchak, and Neeraj Gupta. 2009. "Reactive Transport Modeling of CO_2 and SO_2 Injection into Deep Saline Formations and Their Effect on the Hydraulic Properties of Host Rocks." *Energy Procedia* 1 (1): 3283–90. https://doi.org/10.1016/J.EGYPRO.2009.02.114.

Beckingham, Lauren E., Elizabeth H. Mitnick, Carl I. Steefel, Shuo Zhang, Marco Voltolini, Alexander M. Swift, Li Yang, et al. 2016. "Evaluation of Mineral Reactive Surface Area Estimates for Prediction of Reactivity of a Multi-Mineral Sediment." *Geochimica et Cosmochimica Acta* 188 (September): 310–29. https://doi.org/10.1016/J.GCA.2016.05.040.

Bhattacharjee, Nirveek, Arturo Urrios, Shawn Kang, and Albert Folch. 2016. "The Upcoming 3D-Printing Revolution in Microfluidics." *Lab on a Chip* 16 (10): 1720–42. https://doi.org/10.1039/c6lc00163g.

Bourg, Ian C., Lauren E. Beckingham, and Donald J. DePaolo. 2015. "The Nanoscale Basis of CO_2 Trapping for Geologic Storage." *Environmental Science and Technology* 49 (17): 10265–84. https://doi.org/10.1021/acs.est.5b03003.

Cai, Rong, W. Brent Lindquist, Wooyong Um, and Keith W. Jones. 2009. "Tomographic Analysis of Reactive Flow Induced Pore Structure Changes in Column Experiments." *Advances in Water Resources* 32 (9): 1396–1403. https://doi.org/10.1016/J.ADVWATRES.2009.06.006.

Clark, Elyse V., W. Lee Daniels, Carl E. Zipper, and Kenneth Eriksson. 2018. "Mineralogical Influences on Water Quality from Weathering of Surface Coal Mine Spoils." *Applied Geochemistry* 91 (April): 97–106. https://doi.org/10.1016/J.APGEOCHEM.2018.02.001.

Fuchs, Samantha J., D. Nicholas Espinoza, Christina L. Lopano, Ange-Therese Akono, and Charles J. Werth. 2019. “Geochemical and Geomechanical Alteration of Siliciclastic Reservoir Rock by Supercritical CO_2-Saturated Brine Formed during Geological Carbon Sequestration.” *International Journal of Greenhouse Gas Control* 88 (September): 251–60. https://doi.org/10.1016/J.IJGGC.2019.06.014.

Han, Daehoon, Zhaocheng Lu, Shawn A. Chester, and Howon Lee. 2018. “Micro 3D Printing of a Temperature-Responsive Hydrogel Using Projection Micro-Stereolithography.” *Scientific Reports* 8 (1): 1963. https://doi.org/10.1038/s41598-018-20385-2.

Haug, T. A., I. A. Munz, and R. A. Kleiv. 2011. “Importance of Dissolution and Precipitation Kinetics for Mineral Carbonation.” *Energy Procedia* 4: 5029–36. https://doi.org/10.1016/j.egypro.2011.02.475.

Hughes, Richard John. 1958. “Mississippi State Geological Survey: Kemper County Geology” 84.

Ishutov, Sergey, Franciszek J. Hasiuk, Dawn Jobe, and Susan Agar. 2018. “Using Resin-Based 3D Printing to Build Geometrically Accurate Proxies of Porous Sedimentary Rocks.” *Groundwater* 56 (3): 482–90. https://doi.org/10.1111/gwat.12601.

Jung, Heewon, and Alexis Navarre-Sitchler. 2018. “Scale Effect on the Time Dependence of Mineral Dissolution Rates in Physically Heterogeneous Porous Media.” *Geochimica et Cosmochimica Acta* 234 (August): 70–83. https://doi.org/10.1016/J.GCA.2018.05.009.

Kong, Lingyun, Mehdi Ostadhassan, Xiaodong Hou, Michael Mann, and Chunxiao Li. 2019. “Microstructure Characteristics and Fractal Analysis of 3D-Printed Sandstone Using Micro-CT and SEM-EDS.” *Journal of Petroleum Science and Engineering* 175 (April): 1039–48.

https://doi.org/10.1016/J.PETROL.2019.01.050.

Landrot, Gautier, Jonathan B. Ajo-Franklin, Li Yang, Stefano Cabrini, and Carl I. Steefel. 2012. "Measurement of Accessible Reactive Surface Area in a Sandstone, with Application to CO_2 Mineralization." *Chemical Geology* 318–319: 113–25. https://doi.org/10.1016/j.chemgeo.2012.05.010.

Ligon, Samuel Clark, Robert Liska, Jürgen Stampfl, Matthias Gurr, and Rolf Mülhaupt. 2017. "Polymers for 3D Printing and Customized Additive Manufacturing." *Chemical Reviews* 117 (15): 10212–90. https://doi.org/10.1021/acs.chemrev.7b00074.

Liteanu, Emilia, and Christopher J. Spiers. 2009. "Influence of Pore Fluid Salt Content on Compaction Creep of Calcite Aggregates in the Presence of Supercritical CO_2." *Chemical Geology* 265 (1–2): 134–47. https://doi.org/10.1016/J.CHEMGEO.2008.12.010.

Molins, Sergi, David Trebotich, Li Yang, Jonathan B. Ajo-Franklin, Terry J. Ligocki, Chaopeng Shen, and Carl I. Steefel. 2014. "Pore-Scale Controls on Calcite Dissolution Rates from Flow-through Laboratory and Numerical Experiments." *Environmental Science and Technology* 48 (13): 7453–60. https://doi.org/10.1021/es5013438.

Pashin, Jack C, Denise J Hills, David C Kopaska-merkel, and Marcella R Mcintyre. 2008. "Geological Evaluation of the Potential for CO_2 Sequestration in Kemper County , Mississippi Prepared By."

PHREEQC (Version 3)–A Computer Program for Speciation, Batch-Reaction, One-Dimensional Transport, and Inverse Geochemical Calculations

Qin, Fanqi, and Lauren E. Beckingham. 2019. "Impact of Image Resolution on Quantification of

Mineral Abundances and Accessible Surface Areas." *Chemical Geology* 523 (September): 31–41. https://doi.org/10.1016/j.chemgeo.2019.06.004.

Rathnaweera, T. D., P. G. Ranjith, and M. S. A. Perera. 2016. "Experimental Investigation of Geochemical and Mineralogical Effects of CO_2 Sequestration on Flow Characteristics of Reservoir Rock in Deep Saline Aquifers." *Scientific Reports* 6 (1): 19362. https://doi.org/10.1038/srep19362.

Rusling, James F. 2018. "Developing Microfluidic Sensing Devices Using 3D Printing." https://doi.org/10.1021/acssensors.8b00079.

Srivastava, Sunil Kumar, and AL Ramanathan. 2018. "Assessment of Landfills Vulnerability on the Groundwater Quality Located near Floodplain of the Perennial River and Simulation of Contaminant Transport." *Modeling Earth Systems and Environment* 4 (2): 729–52. https://doi.org/10.1007/s40808-018-0464-7.

Steefel, Carl I, Sergi Molins, and David Trebotich. 2013. "Pore Scale Processes Associated with Subsurface CO_2 Injection and Sequestration." *Reviews in Mineralogy & Geochemistry* 77: 259–303. https://doi.org/10.2138/rmg.2013.77.8.

Teehera, Kimberly B, Sean P Jungbluth, Bogdan P Onac, Tayro E Acosta-Maeda, Eric Hellebrand, Anupam K Misra, Andreas Pflitsch, et al. 2018. "Cryogenic Minerals in Hawaiian Lava Tubes: A Geochemical and Microbiological Exploration." *Geomicrobiology Journal* 35 (3): 227–41. https://doi.org/10.1080/01490451.2017.1362079.

Waldmann, Svenja, Andreas Busch, Kees van Ojik, and Reinhard Gaupp. 2014. "Importance of Mineral Surface Areas in Rotliegend Sandstones for Modeling CO_2–Water–Rock Interactions." *Chemical Geology* 378–379 (June): 89–109.

https://doi.org/10.1016/J.CHEMGEO.2014.03.014.

Watson, Francesca, Julien Maes, Sebastian Geiger, Eric Mackay, Mike Singleton, Thomas Mcgravie, Terry Anouilh, et al. 2018. “Comparison of Flow and Transport Experiments on 3D Printed Micromodels with Direct Numerical Simulations.” *Transport in Porous Media*. https://doi.org/10.1007/s11242-018-1136-9.

www.openfoam.org (Accessed 20 December 2017)

Zhang, Liwei, Yee Soong, Robert Dilmore, and Christina Lopano. 2015. “Numerical Simulation of Porosity and Permeability Evolution of Mount Simon Sandstone under Geological Carbon Sequestration Conditions.” *Chemical Geology* 403: 1–12. https://doi.org/10.1016/j.chemgeo.2015.03.014.

Zhang, X, J Salemans, C J Peach, and C J Spiers. 2002. “Compaction Experiments on Wet Calcite Powder at Room Temperature: Evidence for Operation of Intergranular Pressure Solution.” Edited by S de Meer, M R Drury, J H P de Bresser, and G M Pennock. *Deformation Mechanisms, Rheology and Tectonics: Current Status and Future Perspectives*. Geological Society of London. https://doi.org/10.1144/GSL.SP.2001.200.01.02.

Chapter 4: Conclusions and contribution to new knowledge

4.1 New method to improve understanding of geochemical reaction rates.

3D printing was explored as a means to create replicate natural porous samples with similar properties (Chapter 2). Polymers (HIPS and ABS) were tested for acid resistivity and HIPS was found to be more acid resistant as compared to ABS. Filaments were prepared with mixture of polymer (HIPS) and reactive mineral (calcite) in known weight fractions, though the maximum amount of mineral that can be used in the filament is restricted to 15-20%. A 3D mesh, corresponding to grains, was generated using X-ray CT images of a real sample and used for 3D printing samples. Samples were printed with the novel calcite containing filaments using a fused deposition modelling based 3D printer. Printed samples were analyzed using SEM-BSE and X-ray CT imaging to compute the calcite distribution and mineral accessible surface area. 3D printed samples had accessible calcite surface areas comparable to real samples. Thus, 3D printing was found to be feasible for fabricating samples with accessible mineral surface areas that agree with those of real samples.

4.2 Pore scale variation of ion concentration in porous media using OpenFOAM

Flow and transport of ions was simulated in a mesh representing the pore space in a sandstone sample (Chapter 3). The mesh was generated from X-ray CT images of the sandstone sample

From the Paluxy formation in Kemper County, Mississippi which would be subjected to CO_2 injection. The numerical problem was implemented in OpenFOAM, an open source CFD software. A steady state field was generated for flow, pressure and concentration of ions (Ca^{+2}, H^+ and HCO_3^-). Results from the flow simulation pointed towards presence of a preferential flow path. Different regions in the mesh had different concentration attributing to the heterogeneity present in the pore structure. The effects of advection and diffusion were also observed in areas with high and low velocity respectively. Here, OpenFOAM was used to understand pore scale concentration distribution of ions in Paluxy formation when subjected to CO_2 injection.